Hydrodynamic Controls on Sedimentology and Geomorphology of Marine-Carbonate Ramps: Insights from a Holocene Analogue, Northern Yucatán Shelf, Mexico

By

Thomas C. Neal

Submitted to the graduate degree program in Geology and the Graduate Faculty of the University of Kansas in partial fulfillment of the requirements for the degree of Master of Science.

_____

Chair Dr. Eugene Rankey

_____

Dr. Evan Franseen

_____

Dr. Greg Ludvigson

_____

Dr. Christian Appendini

Date Defended: 23 April 2020

The Thesis Committee for Thomas C. Neal
certifies that this is the approved version of the following thesis:

Hydrodynamic Controls on Sedimentology and Geomorphology of Marine-Carbonate Ramps: Insights from a Holocene Analogue, Northern Yucatán Shelf, Mexico

_____
Chair Dr. Eugene Rankey

Date approved: 11 May 2020

Abstract

As one of the end-members of carbonate platform types, carbonate ramps have long been characterized and interpreted with regard to large-scale controls such as tectonics, sea level, climate, and biota. Yet, details on the impacts of oceanographic processes on facies patterns of ramps remains uncertain. To explore these understudied processes, this study examines carbonate ramp dynamics by integrating *in situ* field measurements, remote sensing data, and hydrodynamic modeling of the Holocene northeastern Yucatán Shelf, Mexico. The goal is to better understand the links between geomorphic and sedimentologic variability and the physical and chemical oceanographic forces of the nearshore areas of ramp systems.

The results reveal how sediment production and accumulation are influenced by the complex interactions of the physical, chemical, and biological processes on the ramp. Upwelled, cooler nutrient-rich waters are transported westward across the ramp and concentrated along the shoreline by cold fronts, westerly regional currents, and longshore currents. This influx supports this transitional heterozoan and photozoan grain association. Persistent trade winds, periodic tropical storms and winter storms generate waves that propagate onto shoreface. This mixed energy, wave-dominated ramp system includes lagoon, barrier island, and upper shoreface geomorphic environments. Extensive shore-parallel sand bodies (beach ridges and subaqueous dune fields) of the high-energy upper shoreface and foreshore are composed of fine to coarse skeletal sand, lack mud, and includes highly abraded, broken and bored grains. The large shallow lagoon is also mixed energy, wave-dominated near the opening to the shoreface, transitioning to tide dominated in the more protected central and eastern regions. Lagoon sediment consists of *Halimeda*-rich muddy gravel and sand. Hydrodynamic forces are especially strong where

bathymetry focuses water flow, as along the promontory and at the lagoon opening, and forming large subaqueous dunes.

Explicit comparison with conceptual numerical models and other shoreface systems demonstrate the influences of hydrodynamics across a wider spectrum of settings. Results reveal that sediment transport patterns are determined by wave height and direction relative to the shoreface, and tidal forces locally control geomorphic and sedimentologic character. Similarly, the physical oceanographic processes that occur throughout the year (e.g. daily tides, episodic winter Nortes, and persistent easterly winds and waves) have more impact on ramp geomorphology and sedimentology than infrequent hurricanes.

Overall, this study provides perspectives on how upwelling and nutrient levels, and hydrodynamic forces influence the varied geomorphic and sedimentologic character of the nearshore areas of this Holocene high-energy carbonate ramp system. These results also provide for more accurate and realistic conceptual models of the depositional variability for a spectrum of modern and ancient ramp systems.

Acknowledgements

This study was funded through the Kansas Interdisciplinary Carbonate Consortium (KICC). Research grants from Geological Society of American and the ExxonMobil Corporation, American Association of Petroleum Geologists and the Society for Sedimentary Geology further supported this study. First, I thank my advisor, Dr. Gene Rankey for all his time, support, guidance, and patience. I would also like to thank my committee members Dr. Christian Appendini, Dr. Evan Franseen, and Dr. Greg Luvigson.

A special thanks to Dr. Rodrigo Garza-Perez for his logistical support for planning and conducting the field research, generating bathymetric data and maps, and supporting my follow-on visit to UMDI-Sisal of UNAM. I am also very grateful and thankful for the field support by LIPC-Sisal, lead by Dr. Appendini and José López-González in the collection of oceanographic data. providing the ADCP meter deployment, retrieval, and data processing as well as conducting the bathymetric survey of the study area. Thanks to Mr. Tom Foster and DHI for use and technical support of the DHI Mike 21 Suite of software that made the hydrodynamic modeling aspects of this research possible. Additionally, thanks to all the field assistants who supported the research in the Yucatán, Jennifer Lowery, Bethany Winkel, and Ana Molina-Hernandez. I would also like to especially thank my colleagues in our research group at KU for all their technical and moral support: Michelle Mary, Jennifer Lowery, Steven Herbst, Abdul Wahab, Adrienne Duarte, Hannah Hubert, Hamilton Goodner, and Bill Mynatt.

Finally, I would like to thank my wife Mary Neal for her endless support, encouragement, and patience.

Table of Contents

List of Figures

List of Tables

Introduction

One of the end-members of carbonate platform types along with isolated platforms and rimmed shelves (Read 1985; Handford and Loucks 1993; Pomar 2001), carbonate ramps are common throughout the geological record, and many contain important hydrocarbon resources. Although carbonate ramps have long been described, categorized, and discussed in literature and interpreted in terms of tectonics, sea level, climate, and biota (summarized in Ahr 1973, Read 1985, Burchette and Wright 1992, Pomar 2001), the details of factors controlling the depositional profiles and facies patterns on ramps remain uncertain (Pomar 2001). Without a protective reef or rim, ramps are subjected to strong physical oceanographic forces (hydraulic energy levels) (James 2010), especially in the shallow-water areas of the upper shoreface and foreshore. As such, carbonate ramps share similar geomorphologies and physical attributes as siliciclastic shelves since they are affected by the same physical oceanographic forces (Burchette and Wright 1992, James 2010).

Study of Holocene systems provides one means to explore dynamics of carbonate ramps. In modern carbonate systems, *in situ* measurements, remote sensing data, and hydrodynamic modeling simulations can facilitate the characterization of the geomorphic and sedimentologic variability to better quantify the interacting physical and chemical oceanographic forces. Commonly cited modern carbonate ramps include the Arabian Gulf (Purser 1973, Alsharhan and Kendall 2003), South Australia (James et al. 2001, Bourman et al. 2016), Mauritania Shelf (Westphal et al. 2010) and the Yucatán ramp. Of these, the Yucatán ramp system has been studied only sparsely (with notable exceptions of Logan 1969; Ward 1985, Gischler and Lomando 2005, Lowery and Rankey 2017).

In this context, the purpose of this study is to explicitly test the hypothesis that hydrodynamics and bathymetry directly influence sediment characteristics (size, sorting and type) and geomorphology of carbonate ramps. This field and hydrodynamic modeling study of the Holocene carbonate ramp near Isla de Holbox, northeastern Yucatán (Mexico), integrates remote sensing, field, petrographical and granulometrical observations of surficial modern sediments with oceanographic observations and hydrodynamic modeling simulations. The aim is to provide qualitative and quantitative perspectives for predicting the spatial variability of sediment accumulations on the nearshore areas of ramp systems. These results provide for more accurate and realistic conceptual models of depositional variability for a spectrum of both modern and ancient ramp systems.

Background

The Yucatán Peninsula of southeastern Mexico is an expansive karst plain of Pleistocene and older carbonate bedrock. Adjoining the Yucatán Peninsula, the broad submerged Yucatán ramp, also known as the Campeche bank (Ahr 1973), extends 245 km north and 200 km west of the peninsula (Fig. 1A). The Yucatán ramp is distally steepened, with slope gradients 0.01º to 0.06º to the west and north before dropping into the abyssal Gulf of Mexico at depths of 80 to 200 m (Fig. 1A). This north-facing distally steepened ramp morphology transitions north of Cancún to an east-facing, narrow, rimmed shelf on Caribbean coast (Fig. 1A).

The focus of this study lies along the northeastern coast of the Yucatán Peninsula (Fig. 1A). It includes Laguna de Yalahau, a large (300 km^2) and shallow (< 4 m depth) protected muddy lagoon with a mangrove fringe (Fig. 1B, C). The lagoon connects to the Gulf of Mexico by a shallow (< 3 m depth), 10 km wide opening to the northwest. The lagoon is enclosed to the north and east by Isla de Holbox, a long (30 km) and narrow (1.5 - 3 km) barrier island that strikes 25

km east to west, but bends to strike northeast to southwest ~ 10 km from its western extremity (Fig. 1B). The study focuses on the foreshore, the gently dipping (0.014º) and shallow (< 9 m depth) upper shoreface within 15 km of the shoreline, and the western areas of the lagoon connecting to the shoreface (Fig. 1C). Offshore from the study area, sheets of carbonate sand cover much of Yucatán ramp, although areas of exposed bedrock are common, along with a few widely scattered reefs (Logan 1969). Lacking pronounced surface water drainage, the peninsula transports negligible siliciclastic sediment into the adjacent the Gulf of Mexico or Caribbean Sea, and carbonate sediment dominates (Logan 1969).

Located in the tropics, the region has a tropical climate with dry winters and wet summers, and an annual rainfall of ~900 mm. Throughout most of the year, trade winds blow from east to west. Over the past 30 years, the winds average 5.5 m/s from the east-northeast, and the waves average 0.9 m significant wave height (H_s), from the northeast (Fig. 2A, B). Stronger winds and larger waves occur during tropical storms (summer and early fall), and when winter cold fronts ("Nortes") pass over the region. Tropical storms and Nortes generate an average of 15 'events' (>2.5 m H_s) per year. Storm waves impact the shoreface primarily from the north and northwest, roughly perpendicular to the coastline. The microtidal tides have a mixed diurnal and semidiurnal regime with a range of 0.1 m neap to 0.5 m spring tide (Cueva-Jimenez and Eáun-Avila 2009).

The area is also influenced by regional currents. The Yucatán Current flows north along Mexico's Caribbean coast, continuing off the eastern Yucatán ramp margin. The persistent east-to-west trade winds and the Yucatán Current combine to create and modulate a regional westerly current that flows across the width of the Yucatán ramp (Zavala-Hidalgo et al. 2003, Enriquez et al. 2010, Ruiz-Castillo et al. 2016). North of the study area and in the inner ramp (< 40 m depth), the mean regional current is around 10 cm/sec, less during periods of weak wind (Ruiz-Castillo et

al. 2016). The Yucatán Current also brings cooler (16-20°C), nutrient-rich upwelled waters across the shallow ramp (Fig. 3) (Merino 1997, Enriquez et al. 2010, Ruiz-Castillo et al. 2016). The most intense upwelling occurs May through August, with the cooler water near the coast (Fig. 3D) (Ruiz-Castillo et al. 2016). Upwelled waters contain high levels of dissolved oxygen, nitrates, phosphates and silicates leading to high fertilizing potential (Merino 1997). Upwelled waters are not the only source of nutrients, however, as groundwater from the Yucatán Peninsula also can provide nutrients to the ramp (Enriquez et al. 2010). Despite the lack of a surface drainage system, the peninsula's karst topography provides conduits for groundwater discharge into the coastal zone (Logan 1969, Herrera-Silveira et al. 2004, Bauer-Gottwein et al. 2011). The primary areas of groundwater discharge into the Yucatán ramp occur where regional-scale fracture zones intersect the coastline such as the Chicxulub crater ring at Celstun Lagoon and Dzilam Bravo to the west and the Holbox fracture zone to the east (Bauer-Gottwein et al. 2011, Enriquez et al. 2013). Thus, both upwelled marine waters and groundwater can contribute to the elevated nutrient levels across the Yucatán ramp.

Methods

Satellite imagery reveals the regional physical and chemical oceanographic conditions of the ramp, guiding the selection of field study areas, surficial sediment sampling locations, and placement of hydrodynamic instruments. Moderate Resolution Imaging Spectroradiometer (MODIS) data from 2004 to 2019 show seasonal and episodic fluctuations of sea surface temperatures and chlorophyll-a concentrations (a proxy for nutrient levels) across the Yucatán ramp. QuickBird, RapidEye, and Landsat remote-sensing satellite images reveal the range of nearshore geomorphic elements on the northeastern Yucatán ramp, including lagoon, foreshore, upper shoreface, and subaqueous dunes.

Field observations described the depths, bottom types, organisms, sedimentary structures (physical and biological), and other notable features in nine transects between 4 and 10 km long across the study area. Two hundred and two surficial sediment samples along these transects capture the range of variability in sediment and bottom types among the geomorphic elements. GPS location (positional error estimated at less than two pixels on the multispectral remote-sensing data, or ~5 m) and depth measurements were recorded at each sample location and at 60 additional locations along transects. Sample spacing ranged from 250 to 500 m for shoreface transects and 500 to 1000 m for lagoon transects. The sediments were collected in small (74 ml) plastic vials by free diving, scuba or by ponar grab sampler (during low visibility or rough-water conditions) with samples enclosed at depth to preserve fines.

Granulometric and petrographic lab analyses quantified each sample's grain size, sorting, and relative abundance of the constituent grain types. After drying, samples were sieved using an ATM Sonic Sifter, and each sieve weighed. GRADSTAT software calculated particle size statistics for each sample (Blott and Pye 2001). Folk and Ward (1957) classification describe mean grain size and sorting (better sediment sorting indicated by lower ϕ values). Petrographic analysis of one hundred and five thin sections of unsorted sediment from the range of geomorphic elements provided qualitative descriptions of constituent grain types, level of abrasion and boring, and relative abundance. Visual estimation of grain type relative abundance was conducted under a petrographic microscope using standard comparators (e.g., Flügel 2004). The level of grain abrasion was categorized as unabraded, minorly abraded, moderately abraded, or highly abraded. Due to high levels of abrasion and bioerosion of most grains and the diminutive size of some grains, a large percentage (average ~ 38%) of this unsorted sediment consisted of petrographically unidentifiable or indeterminate skeletal fragments in the thin sections.

To further understand the physical oceanographic forces of the study area, historical oceanographic data, *in situ* measurements, and numerical computer modeling data were analyzed. Due to the lack of nearby oceanographic buoys or land-based weather stations, 30 years of high-resolution oceanographic data from Laboratio de Ingenierí y Procesos Costeros, Instituto de Ingerieria Universidad Nacional Autónoma de México (LIPC UNAM) Gulf of Mexico regional hindcast model was used to determine historical wind and wave information effecting the region (Appendini et al. 2014). In March 2013, LIPC UNAM conducted a bathymetric survey which provided depth and elevation data across the study area. LIPC UNAM also provided two *in situ* Acoustic Doppler Current Profiler (ADCP) meters which measured the waves, water levels and currents for one lunar cycle (February 7 to March 11, 2013) at two locations (upper shoreface and western lagoon) (Fig. 2C).

Expanding beyond the two ADCP meter locations, numerical two-dimensional (2D) hydrodynamic mapping and modeling programs (DHI's MIKE 21 suite of software) allow assessing the spatial and temporal variability of oceanographic forces across the entire study area. Hydrodynamic modeling also provides a means to isolate and analyze the component oceanographic controls (e.g. wave, tides, and currents) interacting inside the study area and to explore a variety of plausible conceptual ramp scenarios (as described below). Bathymetric survey and regional hindcast wind and wave data were the main inputs for the numeric models. The primary DHI software modules used in the workflow includes the following (Table 1). First, the MIKE Zero Flexible Mesh module creates a high-resolution bathymetric flexible mesh and provides the framework for the other software modules. Next, the MIKE 21 Spectral Wave (SW) module simulates the spectral wave transformation of wind and swell generated waves. Finally, using the SW module results as an input, MIKE 21 Flow Model (FM) hydrodynamic module

simulates water level variations and currents in response to the variety of forcing factors (DHI Water and Environment 2017a). Factors in the modules included wave radiation stress, wind shear stress, bed shear stress, barometric-pressure gradient, horizonal eddy viscosity, flood and drying, tides (water levels), and currents (DHI Water and Environment 2017b). Finally, SW and FM results were validated by comparing the simulation-derived waves, currents, and water levels with measured values from *in situ* lagoon and shoreface ADCP meters. Key simulation parameters of the SW and FM modules (Table 1) were adjusted to produce results that aligned with observations. The flexible bathymetric mesh and the validated SW and FM modules formed the base of the following sets of integrated simulations.

The first set of integrated SW and FM simulations analyzed the oceanographic forces impacting the study area coinciding with the ADCP deployment timeframe. They include the base-case (Table 2, simulation A) which best replicates the sum of hydrodynamic forces, and six follow-on simulations (Table 2, simulations B - G) that replicate individual or combined hydrodynamic forces. Analyzing this set of simulations allowed isolation, rigorous evaluation, and interpretation of the impact of each component oceanographic force on the spatial and temporal variations in hydrodynamics. For example, the ratio of FM simulation-derived tidal range (calculated from water levels) and SW simulation-derived H_s across the area provide metrics for estimating spatial patterns in hydrodynamic energy regime classes (e.g. wave-dominated, mixed energy (wave or tide-dominated), or tide-dominated) (adapted from Hayes, 1979, Mulhern et al. 2017).

An additional set of SW and FM simulations included a series of conceptual ramp simulations that altered the oceanographic forces (e.g. wind, wave, and tides), geomorphological setting (e.g. removal of lagoon), and high energy events (e.g. hurricanes and Nortes) (Table 2,

simulations H to P). These simulations represent a variety of geologically plausible ramp settings, intended to facilitate comparisons and provide insight into a larger range of ramps, both modern and ancient. For all simulations, SW and FM parameters (Table 1) were extracted at the same 6,669 mesh locations across the study area to determine the spatial and temporal variations of the hydrodynamic forces among the simulations.

Finally, the field observations, laboratory measurements, and hydrodynamic modeling results were integrated in a Geographic Information System (ArcGIS) to evaluate the geomorphic, sedimentologic, and oceanographic trends. Statistical analyses provided additional details to the distribution, variation and interrelationships between the geomorphology, sedimentologic character, and the hydrodynamic forces across the study area.

Character of the Isla de Holbox Area

Geomorphology and Sedimentology

Bounded by the Yucatán Peninsula to the south, the study area includes the large (40 by 12 km) muddy Laguna de Yalahau, the long and narrow (35 x 2.5 km) Isla de Holbox foreshore and barrier-island system, and the nearshore area extending approximately 15 km onto the Yucatán ramp to the north of the coastline (Fig. 1B, C). Primary geomorphic elements of the study area are the lagoon (including fringing mangroves), foreshore, upper shoreface, and the subaqueous dune fields (a distinct subregion of the upper shoreface) (Fig. 1C). The sedimentological focus here is on the foreshore, upper shoreface (including subaqueous dunes), and the western lagoon near its opening (Fig. 1C), although the central and eastern lagoon were modeled to an extent to ascertain their influence on focus areas (e.g. sediment source, tidal flow, wind wave fetch area). Overall, the diverse range of physiography, bottom types, biota, and hydrodynamics within and

among geomorphic elements are associated with the variable sedimentologic character across the study area (Table 3).

Striking east to west, Laguna de Yalahau encompasses 300 km^2 and is enclosed by Isla de Holbox to the north, and by the Yucatán Peninsula to the east and south (Fig. 1B). To the west, the lagoon is connected to the Gulf of Mexico by a 10 km-wide opening that strikes west-southwest from the tip of Isla de Holbox to the peninsular shoreline (Fig. 1C). Mangrove marshes line most of the lagoon's 100 km-long perimeter (Figs. 1B, C, 4A). The lagoon is shallow, with water depths no more than 3.5 m, deepest in the western tidal channels leading to open water (Fig. 1C, D). The lagoon includes a variety of bottom types and sedimentologic textures (Table 3). *Halimeda* is pervasive and seagrasses are ubiquitous throughout the lagoon (Fig. 4B). Bioturbated *Halimeda*-rich muddy gravel, muddy sand, and gravelly mud cover much of the central and western lagoon, but transition to sand near the lagoon opening (Fig. 4C). Along the lagoon's perimeter, organic-rich mud borders the mangrove marshes in the intertidal zone (Fig. 4A). The poorly to very poorly sorted sediment has a variable grain size distribution with mud and silt fractions ranging from < 1 to 24% (average 5%) (Fig. 5). Although to a lesser extent than on the foreshore and upper shoreface, lagoon grains commonly are broken and micro-bored (Fig. 6A). Compared to the other geomorphic elements, the lagoon has the most abundant *Halimeda*, mud and other organic matter content and the lowest abundance of mollusk and other skeletal grains (Fig. 6A, E). No corals or coated grains were evident in the lagoon (or the other geomorphic elements of the study area).

North of the lagoon, the foreshore and barrier-island system consists of a series of arcuate beach ridges striking to east - west for 25 km. At the Punta Mosquito promontory, the beach ridge orientation changes to northeast - southwest and extends 10 km to the lagoon's opening. The foreshore and beach ridges continue along the peninsular shoreline west of the lagoon opening.

The foreshore dips gently north to the Yucatán ramp upper shoreface (Figs. 1C, 4D). Ranging from 500 to 3,000 m wide, most of the low-lying beach ridges (maximum elevation 4 m) are covered by vegetation, except in the developed areas of the town of Holbox on the western tip of the island (Fig. 4F). The foreshore is composed of horizontal or gently seaward dipping planar-laminated and cross-bedded sediment (Fig. 4D, Table 3). Sediment consists mostly of fine sand (45%) with less abundant larger and finer grains; however, mud- and silt-sized grains are essentially absent from the foreshore (<0.01) (Fig. 5). In contrast with the other geomorphic elements, foreshore sediment has two distinct sorting categories with finer-grained, moderately well-sorted sediment in the seaward-flanking lower intertidal areas and coarser-grained, poorly sorted sediment with large bioclasts (coquina) higher on the foreshore in the supratidal dunes (Fig. 4E, Table 3). The foreshore, upper shoreface, and subaqueous dunes have similar relative abundances of grain type, comprised of, in order from most common to least common, unidentifiable skeletal fragments, mollusks, bedrock (limestone) lithoclasts, and *Halimeda* grains (Fig. 6E). Minor (< 5%) contributors include miliolid and peneropolid foraminifera, echinoderms, red algae, and diatoms (Fig. 6E).

Seaward of the foreshore and the lagoon's opening, the upper shoreface is the subtidal area that extends out to, and beyond, northern extent of the study area (15 km north of Isla de Holbox). Water depths gradually increase northward to 10 m, with gradients between 0.5 and 1.4 m/km (0.03-0.08°) (Fig. 1D). The upper shoreface includes a variety of bottom types and sedimentologic textures (Table 3). The majority of the upper shoreface is covered by carbonate sand. Seagrass beds are common at water depths ranging from 2 to 4 m (Fig. 4G). Limestone bedrock is exposed at several offshore locations, in deeper (4 to 6 m) water, and north of the Punta Mosquito promontory. The amount of physical sedimentary structures is greater than biological sedimentary

structures indicating that the rate of physical reworking of the sediment is greater than biological reworking (Fig. 4I). Most grains in the upper shoreface are extensively broken, highly abraded, and bored (Fig. 6B, C, D), as in the foreshore and subaqueous dune areas.

A 21 km long by 300 to 2,800 m wide expanse of subaqueous dunes are located seaward of the lagoon opening and northwest of the Isla de Holbox. Dune amplitudes range from 0.3 to 1.3 m with the largest and most extensive dunes forming a bar across the lagoon's opening (Figs. 1B, 1C, 4H). Although they lie geomorphically within the upper shoreface, subaqueous dunes have sedimentologic characteristics distinct from the other parts of the upper shoreface (Table 3). Compared to the upper shoreface, the dune sediment is better sorted, slightly finer grained, and the silt and mud fraction virtually absent (less than 0.1%) (Fig. 5). These features suggest slightly higher energy conditions on the subaqueous dunes than other areas of the upper shoreface, as described and discussed in the following oceanography section.

Oceanography

Measurements from two ADCPs provide information on the oceanography of the study area. These instruments recorded data simultaneously from two locations over a full winter lunar cycle, when the easterly trade winds and waves were interspersed with larger Norte wind and wave events from the northwest (Fig. 7). Due to water depth constraints, the lagoon ADCP was located inside the tidal channel near the lagoon opening and likely measured higher energy levels (e.g. current speeds) than the rest of the lagoon. Across the study area, a diurnal tidal pattern predominates during the spring tides (0.8 m amplitude) and a semidiurnal pattern emerges during neap tides (0.2 m amplitude) (Fig. 7A). Although the water levels are similar, the waves and currents vary considerably between the lagoon opening and the upper shoreface, reflecting the

influence of the diurnal and trade winds, winter storms, and the tidal cycles across their respective bathymetries.

In the lagoon, during this period, the waves averaged 0.3 m H_s, had a maximum wave height of 0.7 m, with a mean wave period of 4 s (Fig. 7B). Waves were bi-directional; most waves came from the east, although the largest lagoon waves were from the northwest, during the Nortes (Fig. 7E). The strongest currents (up to 56 cm/s) happened during spring tides when the outgoing water flow of ebb tides were reinforced by the easterly trade winds and waves. In contrast, the weakest currents (~ 5 cm/s) happened at neap tides during Nortes (Fig. 7A - C). Current directions were also bi-directional, flowing to the northwest during ebb tide and to the east during flood tide (Fig. 7G).

Compared to the lagoon, shoreface waves were larger but the currents were weaker. Waves were predominately from the north, with a mean waves 0.4 m H_s, a maximum height of 1.2 m (recorded during a Norte), and the mean wave period of 5 s (Fig. 7B). Shoreface currents predominately flowed to the southwest (parallel to the shoreline) with a depth-averaged mean velocity of 6 cm/s (Fig. 7F). The strongest shoreface currents reached 23 cm/s; these occurred during Nortes coincident with spring flood tides (Fig. 7A - C). Shoreface currents were the weakest (< 1 cm/s), and reversed direction to north and northeast, during periods of light easterly winds and small waves during neap ebb tides.

In summary, waves are smaller and currents are stronger in the lagoon than those on the upper shoreface. At both locations, larger waves occur during Norte storms and in association with strong easterly trade winds. Current speeds in the lagoon were much stronger than on the shoreface, averaging 21 cm/s versus 6 cm/s on the shoreface. As mentioned beforehand, the lagoon ADCP was located in the tidal channel near the opening and it is expected that current speeds in

the rest of the lagoon are much lower. Furthermore, the strongest currents occur with bi-directional currents during spring tides in the lagoon, whereas shoreface currents flow mostly to the southwest. Overall, although wave and tidal forces influence both locations, wave forces predominate on the shoreface with tidal forces more important in the lagoon.

Hydrodynamic Simulations of Part of the Yucatán ramp

ADCP data provide high temporal resolution physical oceanographic information, but are only from two locations. A suite of numerical hydrodynamic simulations provide a different perspective on physical oceanographic processes across the area. The base-case simulation (Table 2, simulation A) approximates the conditions during the ADCP deployment period, with the actual winds, bathymetry, and boundary conditions, and integrates the SW and FM simulations. These simulations reveal spatial and temporal variations of the waves, tides, and currents across the whole study area. Additionally, a range of simulations isolate and simulate individual hydrodynamic processes for the same period (Table 2, simulations B - G), providing the means to assess their influence.

Base-Case Simulation

The base-case SW simulation results reveal that waves vary markedly across the study area. Larger waves are on the more distal areas of the upper shoreface, smaller waves occur inside the lagoon (Fig. 8 A). Waves are bi-directional, propagating from the east and northeast with easterly trade winds, but shift from the north and northwest with Nortes (Fig. 8B, C). On the upper shoreface, Norte-generated H_s average 0.5 to 1 m, waves nearly 50% larger than during easterly trade winds. Additionally, these base-case SW simulations reveal that considerable wave energy propagates across the opening, and into the lagoon's western reaches.

Using base-case SW simulation results as an input, the base-case FM simulation results reveal the complexity and variations of tides and currents across the study area. In the lagoon, during flood (incoming) tides, water enters the lagoon from the north and northeast. Flow is focused primarily through shallow (2 m) channel near tip of Isla de Holbox and, secondarily, through the slightly deeper (3 m) central channel (Figs. 1C, 8D). In contrast, during ebb (outgoing) tides, water exits the lagoon to the west and northwest, with flow focused through the central channel (Fig. 8E). Average shoreface currents range from 5 to 13 cm/s, whereas average lagoon currents vary between 1 and 13 cm/s (Fig. 8F). The strongest average currents (>10 cm/s) occur at the areas north of the Punta Mosquito promontory, along the upper shoreface north of the lagoon opening, and in the western lagoon, south of the termination of Isla de Holbox (Fig. 8F). Currents are bi-directional in the lagoon, flowing west during ebb tides, and east during flood tides (Fig. 8D, E). Shoreface currents are also bi-directional, but the easterly and northeasterly ebb tide currents are weaker than the westerly and southwesterly flood tide currents. Therefore, the prevailing overall direction of the currents on the shoreface is to the west and southwest, whereas there was no prevailing current direction in the lagoon.

Both base-case SW and FM simulation results permit estimating the classes of hydrodynamic energy regime, based on the ratio of tidal range and H_s derived from the base-case SW and FM simulations (adapted from Hayes 1979, Mulhern et al. 2017) (Fig. 9A). Results show the eastern and central lagoon are tide-dominated, with the western lagoon transitioning to a mixed energy, tide-dominated regime. The lagoon opening and most of the proximal upper shoreface is a mixed energy, wave-dominated regime, but transitions to a fully wave-dominated regime on the distal upper shoreface.

These classification results show relative contributions of wave and tidal forces, but do not include the regional current forces, which can be important on the Yucatán ramp. To visualize spatial changes in the influence of these hydrodynamic influences, the component contributions were isolated from waves-only, tide-only, and the regional current-only FM simulations (Table 2, simulations E, B, D respectively). These contributions, quantified as bed shear stress from each component, were re-combined in a blended RGB image. The resultant image (Fig. 9B) shows spatial changes in bed shear stress (color intensity) and force (hue). It reveals that the strongest bed shear stresses occur in the western lagoon reflect primarily tidal forces and in the subaqueous dune field at the opening of the lagoon, which reflect both tidal and wave forces. Equally strong bed shear stresses near the promontory are a combination of wave, tidal, regional current forces. In short, most of the study area has a mixed energy regime, influenced by both wave and tidal forces, but the regional currents play an important role along the upper shoreface.

Comparison of Sedimentologic Characteristics with Hydrodynamic Modeling Results

Relations between sediment and hydrodynamics could be considered to fall along a spectrum. At one end, sediment may have no relation to hydrodynamic energy. Attributes of carbonate sediment produced *in situ* with negligible transport might reflect a situation close to such an end member. On the other extreme, sediment character might be determined solely by hydrodynamic energy; siliciclastic systems may be nearer to this end-member.

To test where the northeastern Yucatán ramp geomorphic elements fall on this continuum, statistical analyses provide insights into the relationships among oceanographic, hydrodynamic, geomorphologic, and sedimentologic datasets. Granulometric and bottom type data from 201 sediment samples and relative abundance of grain types from 101 thin sections were compared with the corresponding geomorphic parameters (e.g., distance from shoreline, water depth) and

hydrodynamic parameters (e.g., mean wave height and direction, wave power, mean current speed and direction, bed shear stress) derived the base-case hydrodynamic simulations.

The linear pairwise correlation coefficients (r) between each granulometric, bottom type, and grain type characteristic and the geomorphic or hydrodynamic parameter indicates the strength of the relationship between the two datasets. Larger values (positive or negative) suggest a stronger relation. The data show that most correlation coefficients are less than 0.40, although the statistically significant pairs indicate several fundamental relationships (P values < .05, noted in bold in Table 4). Expanding upon the pairwise correlations, these datasets were queried by multiple linear regression analysis to describe the strength of correlation between one granulometric, bottom type, or grain type characteristic and multiple geomorphic and hydrodynamic parameters (Table 5).

Results reveal that with greater water depth and increased distance from the shoreline, wave height, wave power, and sorting increase whereas sediment < 125 μm decreases. Mean grain size and abundance of grain sizes > 125 μm do not change with water depth or distance from the shoreline. With greater water depth, increased distance from the shoreline, higher waves, and stronger currents, the relative abundance of unidentified skeletal fragments, lithoclasts, and mollusks increase. This contrasts with *Halimeda* which decreases with these parameters. All bottom types have relatively strong and statistically significant relationships with geomorphology and hydrodynamics. Sand and rock bottom abundance increases with distance from shoreline, depth, and waves. Seagrass bottom abundance decreases with distance from shoreline and depth; but seagrass bottom increases with stronger currents. Compared to granulometric characteristics, the grain type relative abundance data and bottom types have stronger relationships with geomorphic and hydrodynamic parameters. In general, statistical data indicate that the

granulometric, grain type, and bottom type characteristics of sorting, abundance of sediment < 125 μm, unidentified skeletal fragments, lithoclasts, mollusks, *Halimeda*, and rock and sand bottom types are the most influenced by geomorphology and hydrodynamics.

Perspectives on Controls on Sedimentological Character of Ramps from Numerical Modeling

The numerical hydrodynamic simulations of the Yucatán ramp provide insights into the physical oceanographic processes across the area, and their relation to bottom type and sedimentological character. These insights are expanded through models that simulate hydrodynamics of a broad range of geologically plausible scenarios that could have been present on ancient carbonate ramps, and to constrain and rule out variables as important in this system. Using the framework and results of the base-case hydrodynamic modeling simulations, along with individual and combined hydrodynamic force simulations based on that (Table 2, simulations A - G), nine 'conceptual ramp' simulations explore a broader range of geologically plausible scenarios (Table 2, simulations H - P).

Conceptual ramp simulations examine: 1-5) the influence of varying the strength of winds and waves, or their directions (Table 2, simulations H – J, L, M). These scenarios mimic shorelines with different orientations relative to the dominant winds or waves; 6) the impact of reversing the regional current direction (Table 2, simulation K), to evaluate the influence of the regional current direction relative to the winds; 7) changes associated with a higher (meso) tidal range (Table 2, simulation N), to assess the impact of tidal amplitude; 8) a continuous shoreline, e.g., removing the lagoon (Table 2, simulation O), to assess its role on hydrodynamics; and 9) high-intensity tropical storms (Table 2, simulation P) to describe the impact of these infrequent, but powerful, events.

Impact of wind and waves. Results from the first five simulations reveal several impacts of varying wind and wave simulations. First, the mean current and sediment transport all flow to the west and southwest, except with the wind and wave simulation in which the directions reverse, and come from the west (Fig. 11A, B, Table 6, simulation H - L). Consequently, the direction of the wind and waves, relative to the shoreline, determines the overall direction of the currents and sediment transport. Second, reducing wind and waves to one half those of the base-case setting (Table 2, simulation L) decrease the size of shoreface waves by 60 to 80 % and weaken currents by 25 to 50 % (Table 6, simulation L). Increasing the wind and waves to twice the strength and size of the mean base-case values (Table 2, simulations H, I, M) increases the size of waves by 5 to 90 % and strengthens currents on the shoreface by 5 to 25 % (Table 6, simulation H, I, M). Therefore, as expected, the larger size of the shoreface waves impacts the mean current speed; increased speed increases the volume and the size of the transported sediment, and the character of the remaining, non-transported sediment.

The third impact of changing wind and waves illustrates the influence of topography on both waves and currents. In the base-case and the east wind and wave simulations (Table 2, simulation A, H), the Punta Mosquito promontory shields the proximal shoreface areas to the west, and reduces the size of waves by 10 to 40% (Table 6, simulation H). In the west wind and wave model (Table 2, simulation I), the opposite occurs; in the proximal shoreface east of Punta Mosquito, the waves reduce in size by 5 to 40% (Table 6, simulation I). Currents also are accentuated near the promontories. In the base-case and the five varying wind and wave simulations (Table 2, simulations A, H – L), the strongest shoreface currents occur just offshore of the Punta Mosquito promontory (Figs. 8F, 11 A, B, Table 6, simulations H - L).

In general, the large variability of wave height and currents among the hydrodynamic model simulations and spatially - within the simulations - is controlled by the direction of the waves relative to the shoreline and by the topography. Waves propagating orthogonal to the shoreface (i.e., the north wind and wave simulation) and parallel to the shoreline have the greatest change in wave height (up to ~ 100% increase from the base-case) throughout the shoreface; these have only minimal impact on the mean current, however. In contrast, simulation with waves that propagate parallel to the shoreline (east and west wind and wave simulations), includes waves increase to a maximum of 40 % from the base-case, as the current increases by 25 %. Currents are the strongest in simulations and locations where the direction of the regional current and the direction of wind and waves are all aligned (east wind and wave simulation) (Fig. 11A, Table 6, simulation H). Conversely, currents are weakened by 15 to 20 % when the wind and wave-driven currents are opposed to the regional current (west wind and wave simulation) (Fig. 11B, Table 6, Simulation I). The impact of topography is that both wave heights and current speeds are increased near promontories, but only waves are reduced appreciably on the shielded down-wind and down-wave side of the promontory.

Impact of the regional current. To explore the hydrodynamic influence of the regional current, the reversed regional current model (Table 2, simulation K) inverted the direction of the regional current, so that it flowed towards the east and northeast. The result of this change is shoreface currents that are weaker (- 5 to 25%), except near the opening, where they are slightly stronger (+ 5%) (Table 6, simulation K). Overall, the prevailing current and sediment transport direction remains to the west and southwest as in the base-case, although the current speed and sediment transport capacity were reduced.

Impact of tides. The next two conceptual ramp simulations (Table 2, simulations N, O) highlight the influence of tidal forces. To simulate ramps with larger tides, the mesotidal range model increases the tidal range to 2.5 m (as compared to the base-case's microtidal range of 0.5 m). Lagoon and opening current speeds increase markedly, up to 2.5 times greater than those in the base-case (Fig. 11C, Table 6, simulation N). Promontory currents decrease slightly, and on the rest of shoreface the currents increase slightly relative to the base-case. Since the waves are essentially the same as in the base-case, the net direction of sediment transport remains to the west and southwest, although the stronger currents likely increase the sediment transport capacity inside the lagoon and at the opening. Compared to base-case and all the other conceptual ramps, the mesotidal range simulation has the strongest currents, and thus includes greater potential for sediment transport. Sediment deposited in these areas would be coarser, have less silt and mud, and be better sorted, and the extent of subaqueous dune fields likely would increase further offshore and to the west along the shoreface.

Several models illustrate hydrodynamic changes as the shoreline passes laterally to the opening, demonstrating its impact. To more completely assess its influence, the next conceptual ramp simulation modeled a continuous shoreline with no lagoon (Table 2, simulation O). During neap tides, the mean currents closely match the base-case. During spring tides, the currents are weaker than the base-case, especially during ebb tides. Overall, the shoreface currents are 25 to 50 % weaker at the opening (where the lagoon would have connected to the shoreline) and 10 to 25 % weaker on the rest of the shoreface of the base-case (Fig. 11D, Table 6, simulation O). Thus, removal of the lagoon and loss of the large daily flow of water and sediment at the opening (e.g., by it filling, or by longshore transport across the opening) likely would reduce the size and the character of the subaqueous dune fields along the shoreface. Comparison with the base-case

highlights how the geomorphic setting can concentrate tidal forces and alter the type and character of sediment, even in microtidal settings. Overall, these two conceptual ramp simulations showcase the influence of tidal forces, especially on the current and sediment transport capacity.

Impact of storms. The conceptual ramp simulation of Hurricane Wilma, coupled with the Nortes modeled by the base-case simulation, demonstrate the impact of storms. High-intensity, low-frequency tropical storms were modeled using data from Hurricane Wilma (Table 2, simulation P), a category 5 tropical cyclone whose high winds generated large waves and strong currents that battered the study area in October 2005. In the simulation, H_s of hurricane-generated waves increased at all locations: relative to the base-case, lagoon waves are over 200 % larger, distal shoreface waves doubles in height, and the proximal shoreface waves exceed the base-case by 50 to 90 % (Fig. 11E, Table 6, simulation P). Mean currents also increased during the hurricane in all locations, from 50 % stronger in the lagoon to 20 % stronger at the promontory (Fig. 11F, Table 6, simulation P). Although the storm generated larger waves and stronger currents, the possible net impact of these forces is subdued because the currents reversed during passage of the hurricane, as winds and waves shifted direction.

To provide perspectives for assessing the impact of hurricanes, the base-case simulation included three Nortes and five periods with strong easterly winds and waves (similar to east wind and wave simulation conditions) in the five-week model period. During these Nortes, mean waves in the shoreface are 30 to 60% larger, but mean currents remain 10 to 25% weaker than those of the base-case. During the strong easterly winds and waves, shoreface mean waves are 5 to 35% smaller, but the mean currents are 5 to 25% stronger than those of the base-case. Comparison with Hurricane Wilma simulation imply that the net hydrodynamic impact of an infrequent, but higher intensity, hurricane would not be much greater than that of a typical winter five-week period.

Although hurricanes can be especially damaging upon foreshore and beach areas, this result suggests that the day-to-day and yearly processes may have a greater overall impact than infrequent but higher energy storms for this mixed-energy shoreface system.

Geomorphology, Sedimentology, and Oceanography of the Northeast Yucatán Shelf: Interpretations

Integrating geomorphic, sedimentologic and oceanographic data with constraints offered by numerical modeling provides insights into the depositional patterns and controls. At the largest scale, regional physical and chemical oceanographic conditions impact the type and amount of carbonate production across the ramp. In terms of chemical oceanography, cooler and nutrient-rich waters along the northern Yucatán Peninsula shoreline reflect the impact of upwelling just east of the study area (e.g., Merino 1997, Enriquez et al. 2010, Ruiz-Castillo et al. 2016; Fig. 3). These conditions favor the heterozoan association flora and fauna, dominated by mollusks, foraminifera, echinoderms, and photozoan association *Halimeda;* the latter is ubiquitous on the shoreface and inside the lagoon. Further evidence of upwelled cooler and nutrient-rich waters is the abundant boring and the lack of coated grains (e.g. ooids) and peloids and hard stony corals in the study area (cf. James 1997, Westphal et al. 2010). This creates an environment that the nutrient and turbidity levels are high enough to suppress most photozoan grain production, but light levels are sufficient for the more tolerant *Halimeda* to flourish. Within this regional setting, the characteristics of the sediment, bottom type, and bathymetry vary considerably across the study area, from lagoon, foreshore, subaqueous dunes, and upper shoreface geomorphic elements. This scale of variability is interpreted to be caused by interacting hydrodynamic forces.

With the bounding conditions set by nutrient and temperature influences, the physical oceanographic processes that impact the high-energy depositional system include several components (Fig. 10). Easterly trade winds, tropical storms, and winter Nortes generate westerly

and southerly propagating waves impacting the shoreline. The westward-flowing regional current, easterly trade winds, waves radiating onshore, and the longshore current keep the cooler, nutrient-rich, and more turbid waters along the coastline. Geomorphology focuses wave and tidal energy at promontories and the lagoon opening. Fine sediment (< 125 μm fraction) is winnowed from the shoreface and large sand bodies form along the foreshore and at the subaqueous dune fields.

These hydrodynamic patterns are reflected in the sediment and bottom types. For example, fine sediment and organic matter accumulates in the lagoon, especially in the shallowest and most protected and lowest energy areas. Similarly, across the lagoon, low-energy conditions are reflected by the prevalence of biological sedimentary structures, and the paucity of physical sedimentary structures. It is only in the western lagoon near its opening that current ripples occur. In these areas, sediment has less mud with more broken and moderately abraded grains, relative to sediment from the central lagoon. Coarser grained sediment (gravel and sand) is located inside the tidal channels where the currents are the strongest. Buffered from the cooler upwelled nutrient-rich waters of the shoreface, the lagoon's warmer shallow waters and low-energy conditions favor increased *Halimeda* production and organic matter abundance, mud and seagrass bottoms, and the poorly sorted muddy sediment.

In contrast, the hydrodynamics and the sedimentology reflect higher energy conditions on the shoreface, although like the lagoon, energy varies along and across the shoreface. Waves, tides, and the regional current impact the shoreface, but waves are the predominant hydrodynamic influence on the upper shoreface (Fig. 9). In this area, waves are large enough, and water depths shallow enough, for wave energy to be imparted to the bottom to generate sediment movement. These processes are reflected by a rate of physical reworking of the shoreface sediment greater than the rate of biological reworking, as indicated by wave ripples present across even the deepest

regions of the study area (Fig. 4I), and supported by hydrodynamic model calculations of horizontal particle velocities and bed shear stress. Wave action sets up the westerly and southwesterly flowing longshore drift along the shoreline. Although waves are the dominant hydrodynamic force, tidal forces also influence sediment on the shoreface, especially near the lagoon opening and around the promontory.

These hydrodynamic distinctions are evident in the sediment attributes. For example, foreshore inter-tidal planar-laminated, seaward-dipping to trough cross-bedded layers (foreshore) transition up into vegetation-stabilized supratidal dunes (e.g., berms). In both settings, poorly sorted mollusk-skeletal gravels (e.g., coquina) occur in association with finer and better sorted skeletal, mollusc, *Halimeda*, and lithoclast-rich deposits; these variances likely reflect the influence of both day-to-day and storm processes.

The gently seaward-dipping, subtidal upper shoreface ranges from 0 to 10 m water depth (at the limits of the study area – it likely extends to greater depth) with a variety of bottom types. Rocky bottoms are exposed in locations where wave, tidal, and currents concentrate (white and light purple areas on Fig. 9B), and effectively sweep sediment from the bottom. The most expansive rocky-bottom area is located upon the slight bedrock high north of Punta Mosquito, but smaller rocky-bottom areas occur sporadically along the upper shoreface. Nonetheless, bare sand covers much of the shoreface, and is composed primarily medium to fine skeletal sands. This sand consists primarily of unidentified skeletal grains, mollusks, and *Halimeda,* but limestone bedrock lithoclasts also are common across the shoreface. Despite this high-energy environment, shoreface sediment is only poorly to moderately well-sorted since, like in most all carbonate systems, the grains are formed *in situ* with a variety of sizes, shapes, and densities. Sediment grains are broken, highly abraded and intensively bored, but despite the grain diminution, fine-fraction sediment is

virtually absent on the shoreface. As in the lagoon, coated grains, peloids and hard corals are absent on the shoreface. Unlike the lagoon, organic matter is rare. Overall, the longshore drift, westerly flowing regional currents, and the tidal forces are interpreted to combine, with a net effect of transporting sediment to the west along the shoreface. In this framework, shoreface wave action agitates and winnows the finer grains, then the net current transports the mud and silt away.

Seagrass beds on the shoreface are located in the transitional areas with the lagoon, along the southeasterly striking section of the barrier island and near the mouth of the lagoon, areas where both wave and lagoon tidal energy mix in the relatively shallow (< 4 m) waters. In the seagrass, the sediment poorly sorted, moderately abraded, and include a greater proportion of silt- and mud-sized grains, relative to other shoreface areas.

A special bottom type of the shoreface is in locations with subaqueous dunes, which occur in an area with a distinct combination of hydrodynamic forces. The largest subaqueous dune field (Fig. 1C) is located where shoreface waves, longshore currents, and lagoon tidal forces are concentrated (Fig. 9B). Shoreface waves (mean H_s of 0.3 to 0.4 m) combine with regional and longshore currents (speeds of 10 cm/s) to transport sediment westerly and southwesterly, paralleling the foreshore. Water and sediment from the lagoon influenced by tides (speeds up to 23 cm/s) flow onto the ramp along the mouth of the lagoon, intermixing with the sediment along the shoreface. The influence of these combined and more intense hydrodynamic forces is reflected in the sediment character - sediment lack silt or mud, are better sorted, are more highly, abraded, and include fewer gravel, very coarse, and coarse sand sized grains, as compared to other shoreface and lagoon geomorphic elements.

Comparison with Siliciclastic Shoreface Systems

Siliciclastic shoreline depositional environments commonly are subdivided by the dominant physical process (fluvial, wave, and tide) (Boyd et al. 1992, Dalrymple 2010). In terms of this sort of classification, the Yucatán nearshore systems are broadly analogous to siliciclastic wave-dominated systems, although important distinctions remain (Table 7). [Additional details of comparisons with other wave-dominated shoreface systems, including heterozoan shelves, photozoan platforms, and siliciclastic shorefaces, are in Appendices I and II.]

One of the fundamental distinctions is that siliciclastic sediment is derived from eroding older rocks, and transported to the location of deposition (James 2010). The grain size of siliciclastics is thus controlled by the grain sizes of the source and the varied transport processes, as modified by abrasion in route to deposition. In contrast, most carbonate sediment originates by growth of organisms *in situ*, have a wide variety of grain sizes, shapes, and densities, and accumulates at or near their origin.

Climate influences the two sediments differently. In general, climate has a strong control on carbonate sediment production by its influence on temperature, salinity, hydrodynamic forces, turbidity, and nutrient-levels, which impacts carbonate-producing organisms. Although climate (e.g. wet vs. dry) impacts the nature of siliciclastic sediment, compared to carbonates, the influence is minor (Dalrymple 2010).

Similarly, the influence of ocean chemistry (e.g. upwelling and elevated nutrient levels) has only minor (if any influence on siliciclastic shoreline systems (Dalrymple 2010)), in contrast to carbonate systems. In carbonates, the level of nutrients (from upwelling and/or runoff from land) and temperature (from upwelling or by latitude) are both major controls on distribution of

heterozoan and photozoan associations in carbonate systems (Hallock and Schlager 1986, James 1997, Pomar et al. 2004, Westphal et al. 2010, Michel et al. 2011, Klicpera et al. 2015).

Finally, physical processes are the primary, if not sole, control on siliciclastic sediment deposition, from origin to transport to deposition. In contrast, physical processes are just one of the many controls on carbonate sediment origin and accumulation.

Nonetheless, physical processes influence the geomorphology similarly in both carbonate and siliciclastic systems. The geomorphic elements are broadly comparable including coastal dunes, sandy foreshores, and sandy upper shorefaces. Longshore transport of sediment form barrier islands and shoreface subaqueous dunes creating protected lagoons and barrier islands (Fig. 12). Sediment, once formed, is transported within the wave-dominated environment according to the laws of physics, resulting in generally similar sedimentary structures. For example, whether carbonate and siliciclastic, foreshores include gently seaward-dipping, laminated units, upper shorefaces have gently inclined and trough cross-bedded units derived from numerous sand bodies (e.g. subaqueous dunes, sheet sands, subaqueous dunes), and lagoons are muddy, rich in seagrass, and lined with mangroves (in tropical to temperate regions). Although theses carbonate and siliciclastic shoreface systems generally are wave-dominated, the impact of tidal energy is pervasive, and contributes to the heterogeneity of the sediment, especially in nearshore areas where tidal forces are focused. A marked contrast between the two systems is that carbonate systems are influenced by the wind and wave direction relative to the shoreline; they include distinct windward versus leeward differences in carbonate production and geomorphology. Finally, in both systems, there are a wide range of scales of the geomorphic elements and their sedimentary structures (Fig. 12).

Despite having broadly comparable geomorphologies, the granulometery differs between the two systems, as they are controlled by distinctly different processes. For carbonates, grain type, size, and shape are determined by the type, size and skeletal structure and durability of calcareous biota inside the environment, as then modified by any transport. In siliciclastic systems, grain type and grain size are shaped by source, transport pathways, and hydraulic energy at deposition (James 2010). Sediment sorting for siliciclastics is also controlled by hydraulic energy at deposition whereas in the carbonate systems sediment not in hydrodynamic equilibrium with ambient conditions can accumulate because it originates there. Common to both wave-dominated systems is the lack of mud in the high-energy shorefaces.

Summary and Conclusions

This study explores the relationships between oceanography and the sedimentology and geomorphology of the nearshore areas of a high-energy, Holocene carbonate ramp of northeastern Yucatán ramp. This mixed energy, but wave-dominated, ramp system includes geomorphic environments including lagoon, barrier island, foreshore, and upper shoreface, and is characterized by carbonate production from both heterozoan and photozoan grain associations. Observations and numerical modeling of the hydrodynamic forces provide insights on the role of complex interaction of physical, chemical, and biological processes on sediment accumulations. Although hydrodynamics and bathymetry influence sediment characteristics (size, sorting and type) and geomorphology of carbonate ramps, they are not the sole control.

Primary controls on geomorphology and sedimentology in this system include the cold fronts, westerly regional currents, and longshore currents that transport upwelled waters westward across the ramp and concentrate the cooler nutrient-rich waters along the coastline. This influx favors the transitional heterozoan and photozoan association. Persistent trade winds, as well as

periodic tropical storms and Nortes, generate waves that propagate onto the shoreface. The resultant high-energy upper shoreface and foreshore includes extensive shore-parallel sand bodies (beach ridges and subaqueous dune fields) dominated by fine to coarse sand that is highly abraded, broken, bored, and lacks mud. The distal upper shoreface also is wave-dominated, but the western lagoon area is a mixed energy system, with prominent wave and tidal forces. Where bathymetry focuses water flow, as in the lagoon opening and along the promontory, tidal forces are especially strong.

Numerical models of conceptual ramps and comparisons with other ramp systems provide insights to the influences of hydrodynamics on a wider spectrum of ramps. Analysis of models with varying combinations of wind and wave direction and intensities reveal that wave size and direction determines overall sediment transport patterns. Other models reveal the location, intensity and impact of tidal forces and demonstrate that large lagoons (and the related water and sediment flux) likely are necessary to produce large offshore subaqueous dune fields. Additionally, the daily to seasonal processes have more influence than infrequent high-energy events (e.g. hurricanes).

Collectively, these results show how the range of hydrodynamic forces along with upwelling and nutrient levels influence the geomorphic and sedimentologic character and variability of the nearshore areas of modern high-energy carbonate ramp system. Results provide conceptual and numerical constraints on fundamental controls on sedimentologic variability of nearshore parts of ramps and insights for more accurate and realistic conceptual models of depositional variability for a spectrum of both modern and ancient carbonate ramp systems.

References

AHR, W.M., 1973, The carbonate ramp an alternative to the shelf model: Transactions Gulf Coast Association of Geological Societies, v. 23, p. 221-225.

ALSHARHAH, A. S., AND KENDALL, C. G. ST. C., 2002, Holocene coastal carbonates and evaporites of the southern Arabian Gulf and their ancient analogues: Earth-Science Reviews, v. 61, p. 191-243.

APPENDINI, C.M., TORRES-FREYERMUTH, A., SALLES, P., LOPÉZ-GONZALÉZ, J., AND MENDOZA, E. T., 2014, Wave climate and trends of the Gulf of Mexico: A 30-yr wave hindcast: Journal of Climate, v. 27, p. 1619-1632.

BAUER-GOTTWEIN, P., GONDWE, B. R. N., CHARVET, G., MARÍN, L. E., REBOLLEDO-VIEYRA, M. AND MEREDIZ-ALONZO, G., 2011, Review: The Yucatán Peninsula karst aquifer, Mexico: Hydrogeology Journal, v. 19, p. 507-524.

BLOTT, S.J., AND PLYE, K., 2001, Gradistat: a grain-size distribution and statistics package for the analysis of unconsolidated sediments: Earth Surface Processes and Landforms, v. 26, p. 1237–1248.

BOURMAN, R.P., MURRAY-WALLACE, C.V., AND HARVEY, N., 2016, Coastal landscapes of South Australia: University of Adelaide Press, p. 387-405.

BURCHETTE, T.P. AND WRIGHT, V.P., 1992, Carbonate ramp depositional systems: Sedimentary Geology, v. 79, p. 3-57.

CISNEROS, R.A., 2011, Provenance and origin of Holocene beach ridge and modern beach sands from the Costa de Nayarit, western Mexico: LSU Master's Theses. 3550. https://digitalcommons.lsu.edu/gradschool_theses/3550

CUEVA-JIMENEZ, A., AND EUÁN-AVILA, J., 2009, Morphodynamics of carbonate beaches in the Yucatán Peninsula: *Ciencias Marinas*, v. 35, p. 307-320.

DALRYMPLE, R.W., 2010, Introduction to siliciclastic facies models, *in* James, N.P., and Dalrymple, R.W., eds, Facies Models 4: Geological Association of Canada, p. 59-72.

DHI WATER AND ENVIRONMENT, 2017a, MIKE 21 – MIKE powered by DHI product flyer: Available from DHI Water and Environment, Denmark.

DHI WATER AND ENVIRONMENT, 2017b, MIKE Zero and MIKE 21 Release 2017 User Guide: Available from DHI Water and Environment, Denmark.

ENRIQUEZ, C., MARIÑO-TAPIA, I.J., AND HERRERA-SILVEIRA, J.A., 2010, Dispersion in the Yucatán coastal zone: Implications for red tide events: Continental Shelf Research, v. 30, p. 127-137.

ENRIQUEZ, C., MARIÑO-TAPIA, I.J., JERONIMO, G., AND CAPURRO-FILOGRASSO, L., 2013, Thermohaline processes in a tropical coastal zone: Continental Shelf Research, v. 69, p. 101-109.

FLÜGEL, E., 2004, Microfacies of carbonate rocks: analysis, interpretation and application: Berlin, Springer-Verlag, p. 976.

FOLK R.L., AND WARD, W.C., 1957, Brazos river bar: a study of significance of grain size parameters: Journal of Sedimentary Petrology, v. 27, p. 3–26.

GISCHLER, E., AND LOMANDO, A.J., 2005, Offshore sedimentary facies of a modern carbonate ramp, Kuwait, northwestern Arabian-Persian Gulf: Facies, v. 50, p. 443-462.

HALLOCK P., SCHLAGER W., 1986, Nutrient excess and the demise of coral reefs and carbonate platforms: Palaios, v. 1. p. 389–398.

HANDFORD, R., AND LOUCKS, R.G., 1993, Carbonate depositional sequences and systems tracts responses of carbonate platforms to relative sea-level change, *in* Loucks, R.G., and Sarg, J.F., eds., Carbonate sequence stratigraphy: Recent advances and applications: American Association of Petroleum Geologists Memoir, v. 57, p. 3-41.

HAYES, M.O., 1979, Barrier island morphology as a function of tidal and wave regime, *in* Leatherman, S.P. ed., Barrier islands from the Gulf of Mexico to the Gulf of St. Lawrence: Academic Press, New York, p. 1–28.

HERRERA-SILVEIRA, J.A., COMIN, F.A., ARANDA-CIREROL, N, TROCCOLI, L., AND CAPURRO, L., 2004, Coastal water quality assessment in the Yucatán Peninsula: management implications: Ocean and Coastal Management, v. 47, p 625-639.

JAMES, N.P., 1997, The cool-water carbonate depositional realm, *in* James, N.P., and Clarke, J., eds, Cool-water carbonates: Society for Sedimentary Geology Special Publication, v. 56, v. 56, p. 1–20.

JAMES, N.P., 2010, Introduction to biological and chemical sedimentary facies models, *in* James, N.P., and Dalrymple, R.W., eds, Facies Models 4: Geological Association of Canada, p. 323-339.

JAMES, N.P., BONE, Y., COLLINS, L.B., AND KYSER, T.K., 2001, Surficial sediments of the Great Australian Bight: facies dynamics and oceanography on a vast cool-water carbonate shelf: Journal of Sedimentary Research, v. 71, no. 4, p. 549-567.

KLICPERA, A., MICHEL, J., AND WESTPHAL, H., 2015, Facies pattern of a tropical heterozoan carbonate platform under eutrophic conditions: the Bank d'Arguin, Mauritania: Facies, v. 51, p. 19-25.

LOGAN, B.W., 1969, Physical environment of Yucatán reefs and banks: *in* Logan, B.W., Carbonate sediments and reefs, Yucatán Shelf, Mexico: American Association of Petroleum Geologists Memoir, v. 11, p. 153-156.

LOWERY, J.G., AND RANKEY, E.C., 2017, Nearshore influences of upwelling, waves and currents on a tropical carbonate ramp: Holocene, northwestern Yucatán Shelf, Mexico: Journal of Sedimentary Research, v. 87, p. 546-566.

MERINO, M., 1997, Upwelling on the Yucatán Shelf: hydrographic evidence: Journal of Marine Systems, v. 13, p. 101-121.

MICHEL, M., VICENS, G.M., AND WESTPHAL, H., 2011, Modern heterozoan carbonates from a eutrophic tropical shelf (Mauritania): Journal of Sedimentary Research, v. 81, p. 641-655.

MULHERN, J.S., JOHNSON, C.L., AND MARTIN, J.M., 2017, Is barrier island morphology a function of tidal or wave regime?: Marine Geology, v. 387, p. 74-84.

PLINT, A.G., 2010, Wave- and storm-dominated shoreline and shallow-marine systems, *in* James, N.P., and Dalrymple, R.W., eds, Facies Models 4: Geological Association of Canada, p. 167-199.

POMAR, L., 2001, Types of carbonate platforms: a genetic approach: Basin Research, v. 13, p. 313-334.

POMAR, L., BRANDANO, M., AND WESTPHAL, H., 2004, Environmental factors influencing skeletal grain sediment associations: a critical review of Miocene examples from the western Mediterranean: Sedimentology, v. 51, p. 627-651.

PURSER, B.H., ED., 1973, The Persian Gulf: Holocene carbonate sedimentation and diagenesis in a shallow epicontinental sea: Berlin, Springer-Verlag, p. 471.

RANKEY, E.C., 2014, Contrast between wave- and tide-dominated oolitic systems: Holocene of Crooked-Acklins Platform, southern Bahamas: Facies, v. 60, p. 405-428.

READ, J.F., 1985, Carbonate platform facies models: American Association of Petroleum Geologists Bulletin, v. 69, no. 1, p. 1-21.

RUIZ-CASTILLO, E., GOMEZ-VALDES, J., SHEINBAUM, J., AND RIOJA-NIETO, R., 2016, Wind-driven coastal upwelling and westward circulation in the Yucatán Shelf: Continental Shelf Research, v. 1118, p. 63-76.

WARD, W.C, 1985, Quaternary geology of northeastern Yucatán peninsula, *in* Weidie, A.E., Ward, W.C., and Back, W., eds., Geology and hydrogeology of the Yucatán and quaternary geology of the northeastern Yucatán Peninsula: New Orleans Geological Society, New Orleans, Louisiana, Part II, p. 23-95.

WESTPHAL, H., HALFAR, J., AND FREIWALD, A., 2010, Heterozoan carbonates in subtropical to tropical settings in the present and in the past: International Journal of Earth Sciences, v. 99, p. S153-S169.

ZAVALA-HIDALGO, J., MOREY, S.L., AND O'BRIEN, J.J., 2003, Seasonal circulation of the western shelf of the Gulf of Mexico using high-resolution numerical model: Journal of Geophysical Research, v. 108, p. 1-19.

Figures

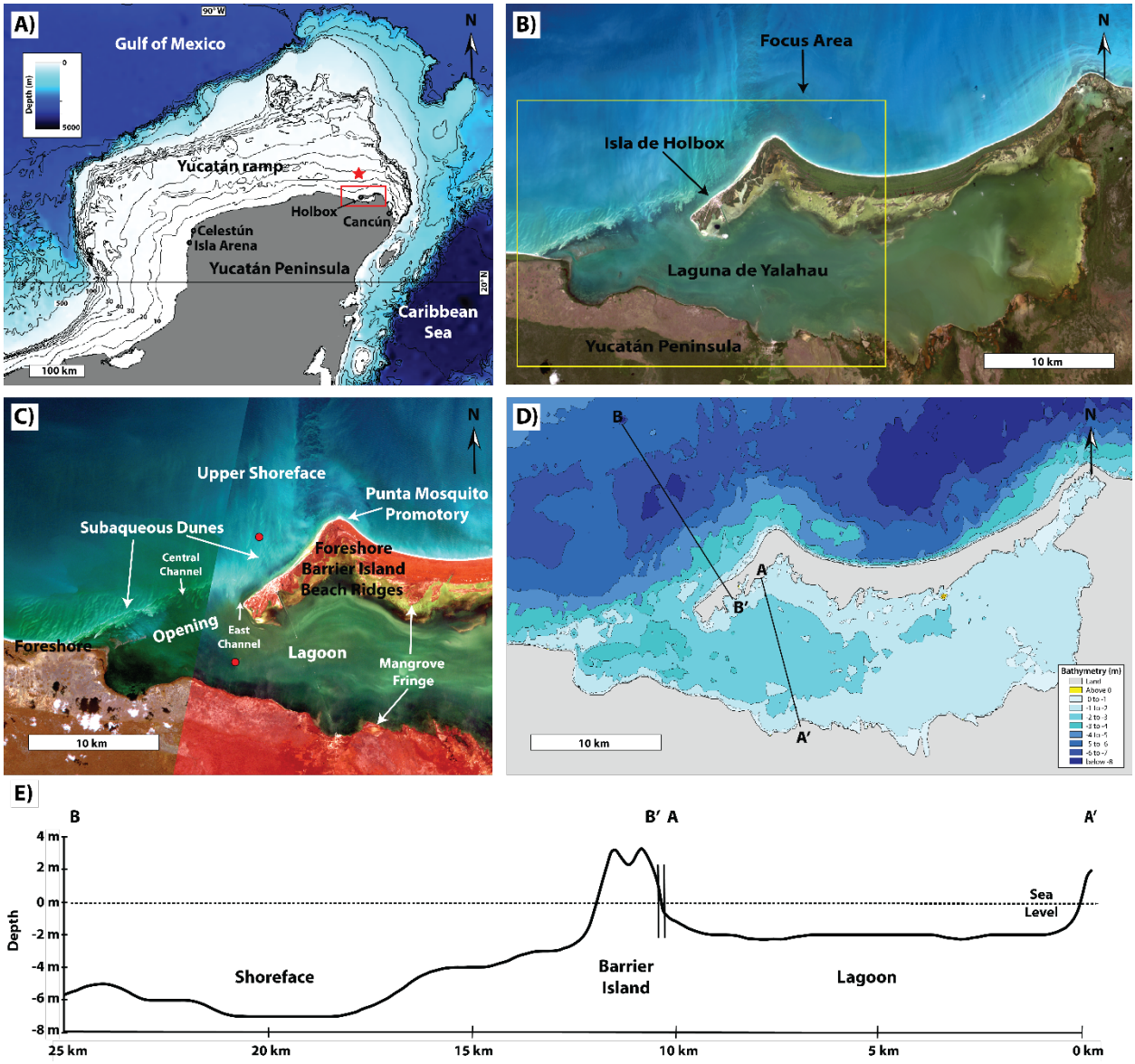

Fig. 1. Geographic location, general geomorphology, and bathymetry of study area. A) Map of Yucatán ramp. Ramp extends 150 to 250 km northward and westward from the Yucatán Peninsula (land, shown in grey) into Gulf of Mexico. Contours are at 10 m depth intervals from 1 to 100 m and at 500 m depth intervals from 500 to 5000 m. Study area is denoted by red rectangle, and the red star shows location of extracted synoptic wind and wave data. B) Remote-sensing image showing the Isla de Holbox and Laguna de Yalahau region. The focus area is highlighted in the yellow box. C) Remote-sensing image of focus area. Note the range of geomorphic elements, including upper shoreface, subaqueous dunes, foreshore barrier island with beach ridges, and the lagoon with mangrove fringe. Red circles indicate deployment locations of in situ current meters. D) Bathymetry of Isla de Holbox focus area. E) Bathymetric profile across shallow (≤2 m) lagoon (A' – A) and the gently dipping (0.014º) shoreface (B' – B).

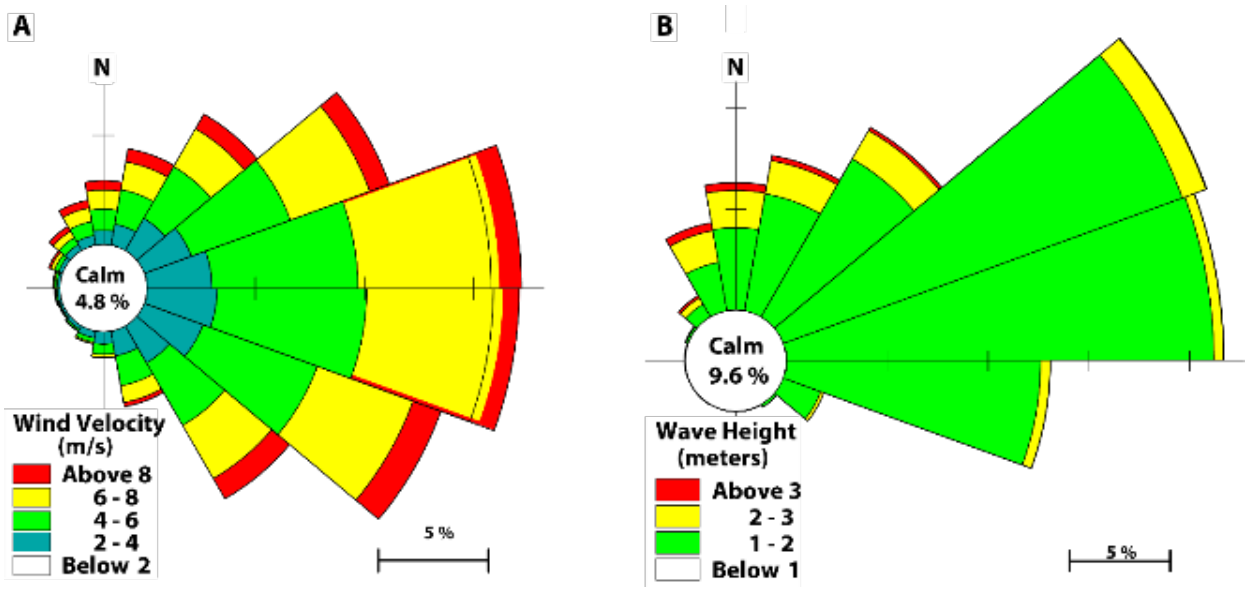

Fig. 1. Wind and wave rose diagrams, data from location indicated by red star in Fig. 1A. These plots indicate wind (A) and wave (B) magnitude, frequency with which they occur, and the direction from which they originate. Diagram data are extracted from Laboratio de Ingenierí y Procesos Costeros, Instituto de Ingerieria Universidad Nacional Autónoma de México 30 year hindcast model dataset of the Gulf of Mexico and Caribbean Sea (Appendini et. al. 2013). A) Wind rose, illustrating directions from which wind blows. Note that the most persistent winds are the easterly trade winds. The highest wind velocities occur during Summer to early Fall tropical storms from the east and during Winter cold fronts (Nortes) from the north and northwest. B) Wave rose, illustrating directions from which waves come. Note that most waves from the east and northeast, but that the largest waves are from the north and northwest, and reflect Nortes.

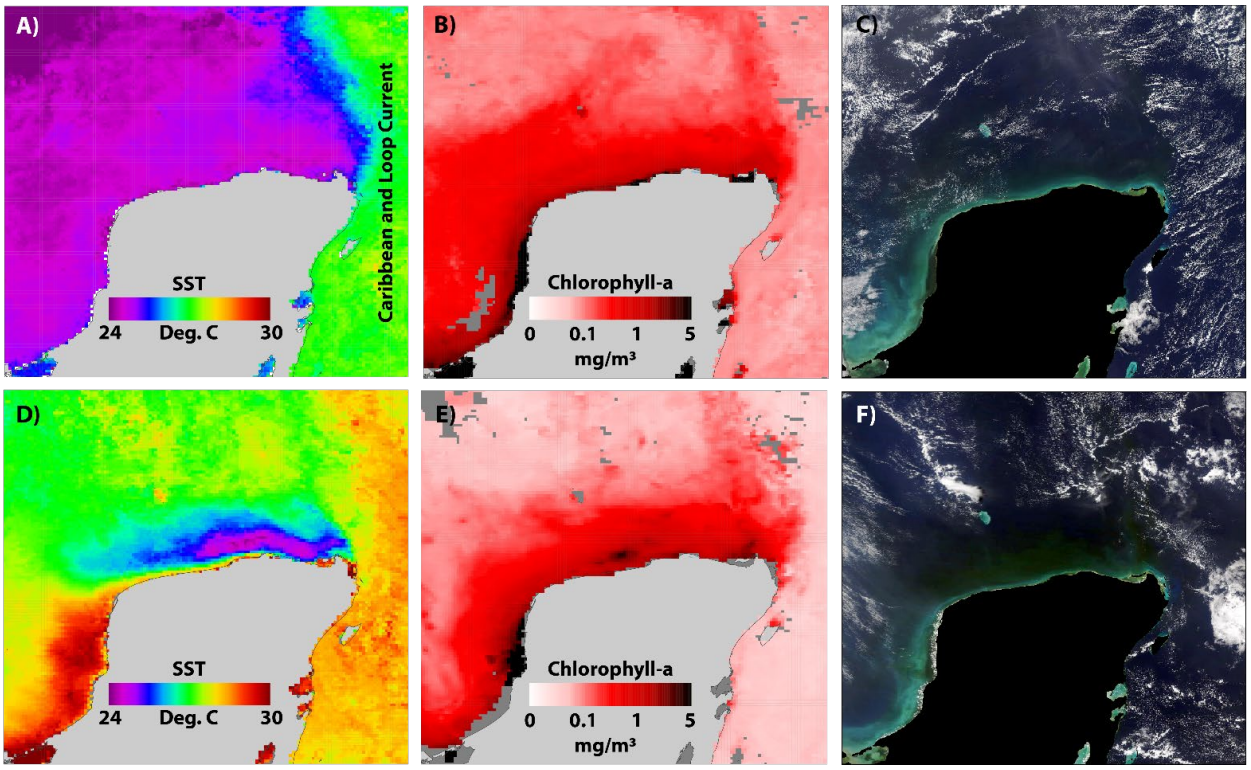

Fig. 2. Variability of sea-surface temperature (SST) and chlorophyll-a (Chl-a, a proxy for nutrient levels), and turbidity, Yucatán ramp area. Plots show representative changes from winter and spring-summer A – C) Representative winter conditions. A) Average monthly SST for January 2015; temperatures range from 24-26°C across the ramp, much cooler than the Caribbean and Loop Current. B) Average monthly Chl-a (log scale) for January 2015. Note that Chl-a is elevated along the northern and western Yucatán coastlines, suggesting high nutrient levels. C) 13 January 2015 visible image revealing high turbidity along the northern and western Yucatán coastlines. D – F) Representative spring-summer conditions. D) Average monthly SST for May 2015 showing cooler ($\leq$ 24°C) upwelled waters along the northern coastline. E) Average monthly Chl-a (log scale) for May 2015. Data show higher Chl-a levels in the cooler upwelled waters (D) especially along the coastline. F) Turbidity is less along the coast during the spring than the winter (28 May 2015 visible image).

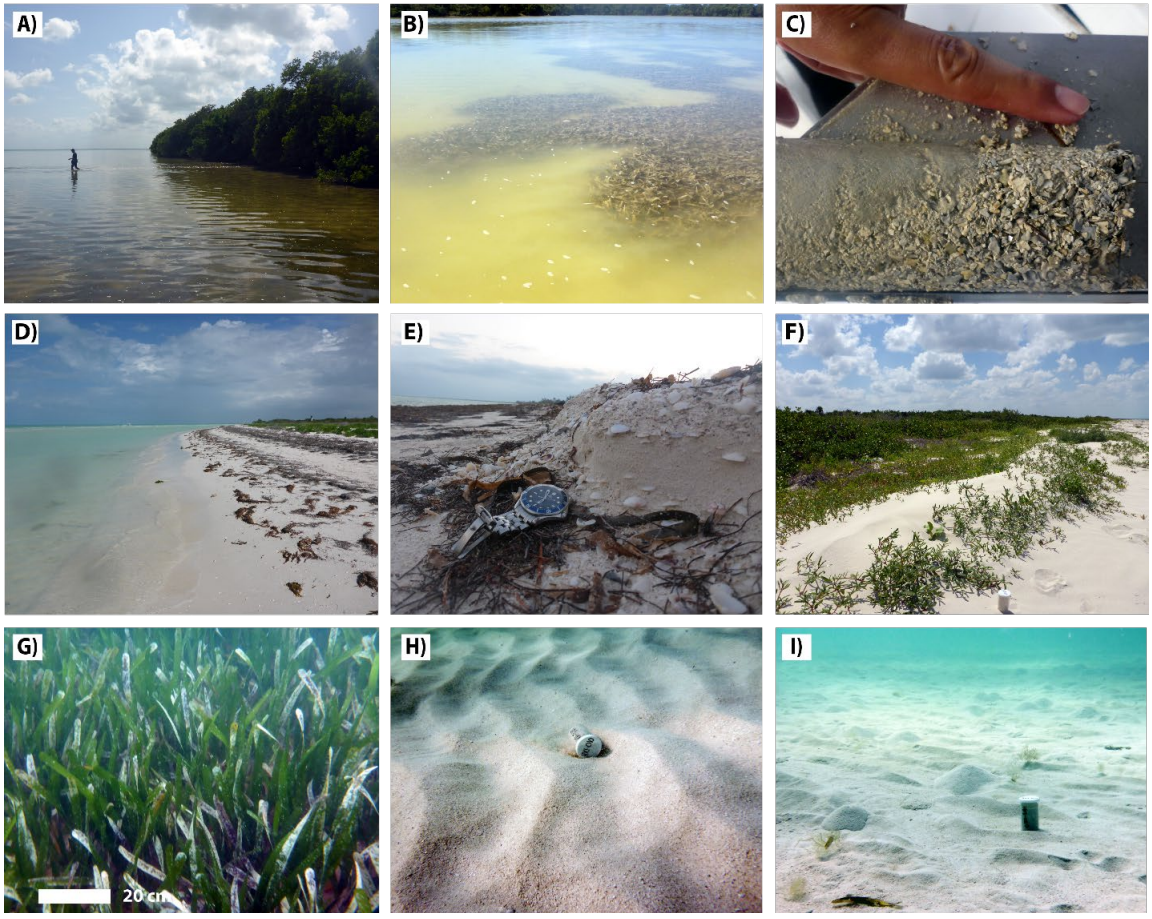

Fig. 3. Field photographs illustrating sedimentologic and bottom type variability of Isla de Holbox study area. A) Mangroves, such as those that fringe the large lagoon. B) Seagrass beds. This bottom type is abundant in the shallow (<1 m) lagoon. C) Shallow core sample of the poorly sorted muddy Halimeda-rich skeletal sand to gravel, sediment that covers most of the lagoon bottom. D) Gently dipping foreshore along Isla de Holbox barrier island. E) Foreshore sediment, including bivalve-rich fine to coarse skeletal sand (4 cm watch face for scale). F) Barrier island consists series of aeolian dunes covered with vegetation. G) Upper shoreface Thalassia testudinum seagrass beds. H) Proximal, shallow (2 m) upper shoreface rippled sand bottom amongst subaqueous dunes, illustrating a paucity of biological sedimentary structures (7 cm sample vial for scale). I) Distal, deep (7 m) upper shoreface sand bottom with both physical (ripples) and biological (e.g. mounds and pits) sedimentary structures (7 cm sample vial for scale).

Fig. 4. Field photographs illustrating sedimentologic and bottom type variability of Isla de Holbox study area. A) Mangroves, such as those that fringe the large lagoon. B) Seagrass beds. This bottom type is abundant in the shallow (<1 m) lagoon. C) Shallow core sample of the poorly sorted muddy Halimeda-rich skeletal sand to gravel, sediment that covers most of the lagoon bottom. D) Gently dipping foreshore along Isla de Holbox barrier island. E) Foreshore sediment, including bivalve-rich fine to coarse skeletal sand (4 cm watch face for scale). F) Barrier island consists series of aeolian dunes covered with vegetation. G) Upper shoreface Thalassia testudinum seagrass beds. H) Proximal, shallow (2 m) upper shoreface rippled sand bottom amongst subaqueous dunes, illustrating a paucity of biological sedimentary structures (7 cm sample vial for scale). I) Distal, deep (7 m) upper shoreface sand bottom with both physical (ripples) and biological (e.g. mounds and pits) sedimentary structures (7 cm sample vial for scale).

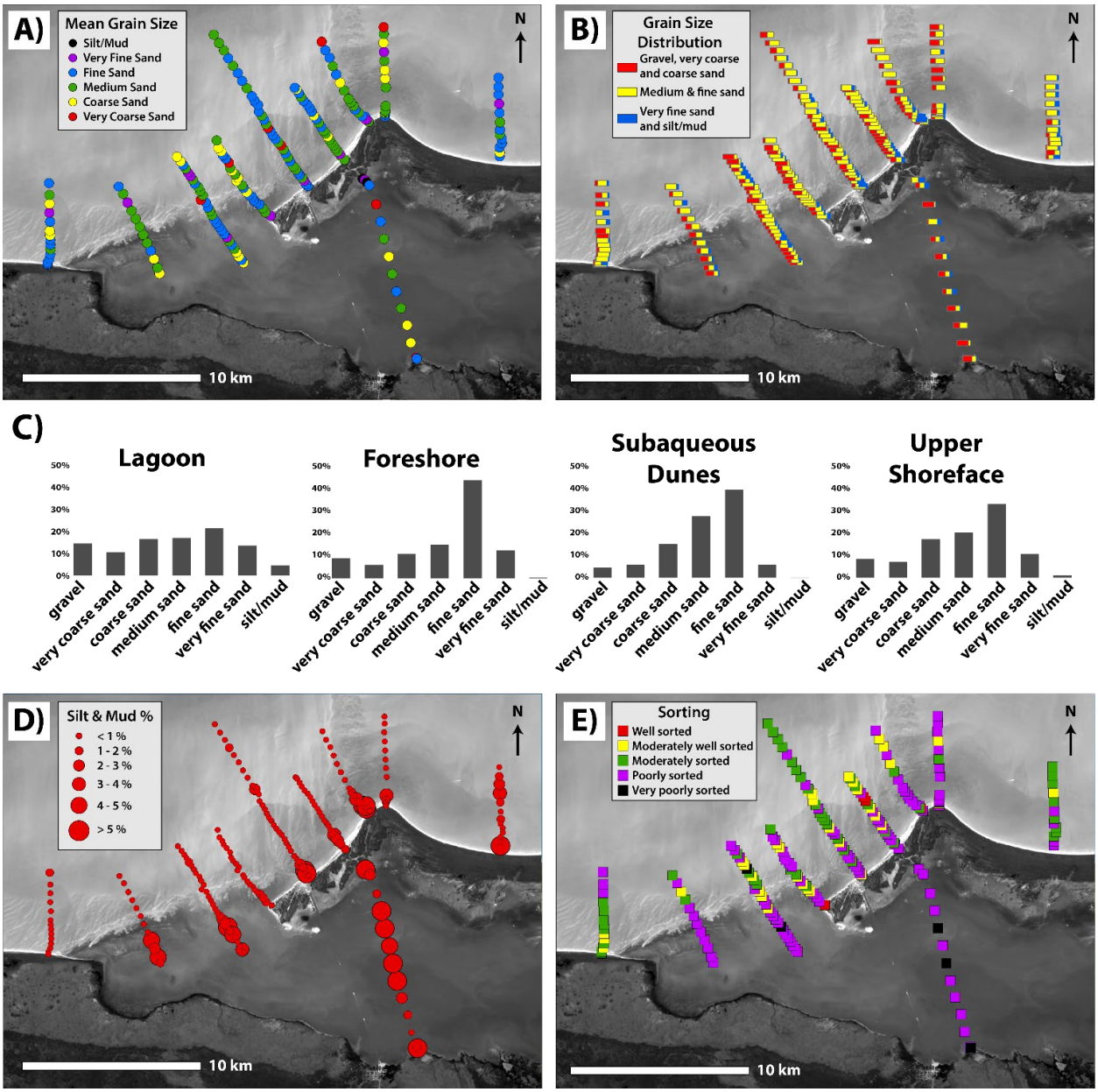

Fig. 7. Granulometric characteristics across the study area. A) Mean grain size of surface sediment. B) Relative proportions of coarse, medium, and fine grain size fractions. C) Mean of grain size distributions by geomorphic element. The foreshore, subaqueous dunes, and upper shoreface have similar mean grain size distributions, with fine sand the modal size. This mode contrasts with the more evenly distributed sizes of the sediment in the lagoon. D) Abundance of silt and mud fraction (< 62 μm). With few exceptions, foreshore and upper shoreface sediment has < 1% mud, whereas the lagoon sediment averages > 5% mud. E) Sorting (Folk & Ward, 1957). In general, lagoon sediment is the least sorted (poorly to very poorly) whereas the subaqueous dunes are the best sorted (moderately well).

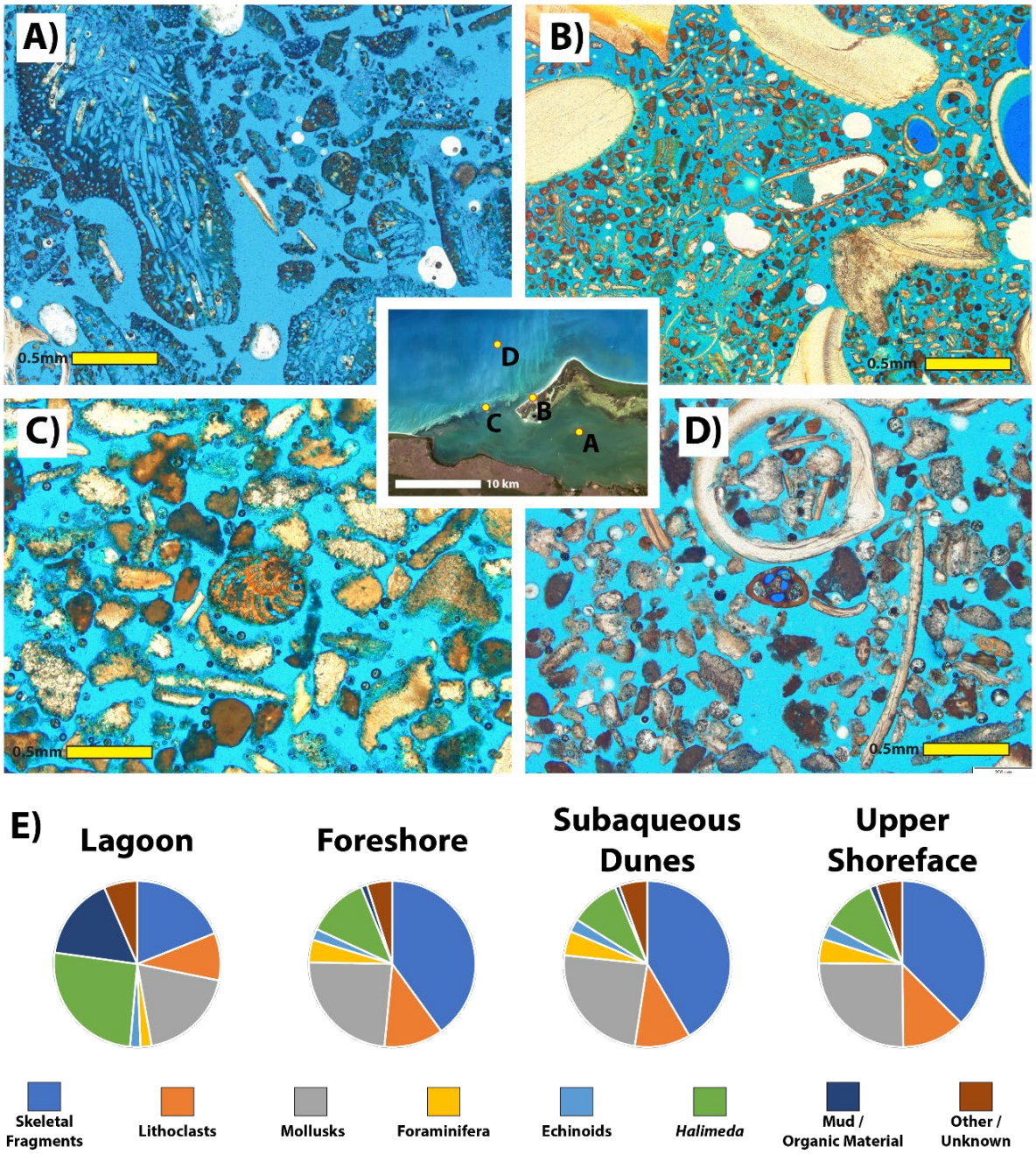

Fig. 8. Representative thin-section photomicrographs illustrating a range of grain types and sizes among each geomorphic element. The remote-sensing image illustrates the location of sample from which each thin section was made (A-D). A) Halimeda-rich muddy gravel from the central lagoon. B) Bivalve-rich skeletal sand with bi-modal size and poor sorting from the foreshore. C) Moderately well sorted, fine to medium skeletal sand from a subaqueous dune. D) Poorly sorted medium skeletal sand from the upper shoreface. Note that most upper shoreface grains are highly abraded and heavily bored. E) Average relative abundance of grain types among the geomorphic elements (n = 105 total samples). In the lagoon, Halimeda is the most abundant constituent. Upper shoreface sediment is composed mainly of unidentified skeletal fragments, mollusks, lithoclasts, and Halimeda.

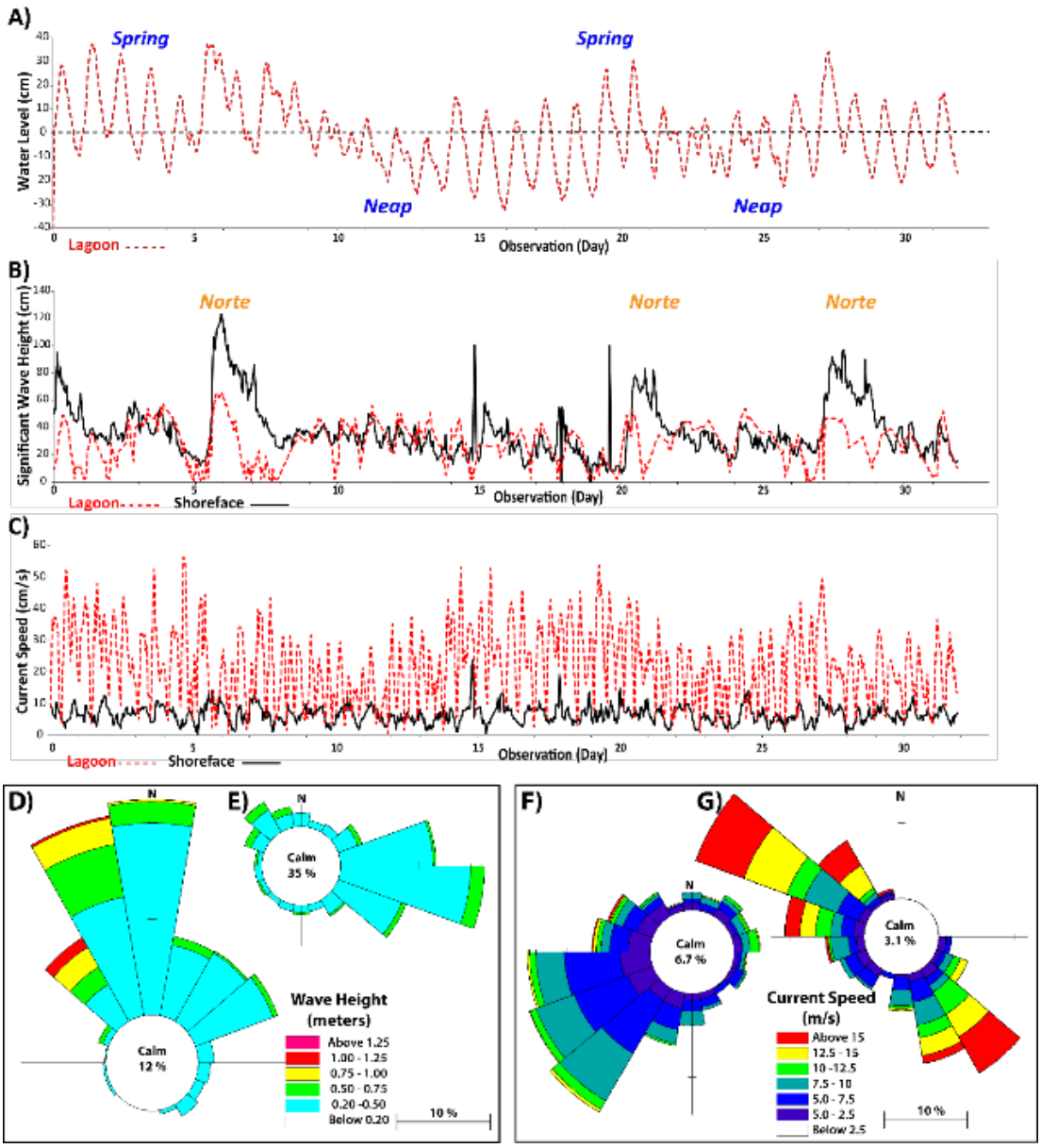

Fig. 9. Hydrodynamics of the upper shoreface and lagoon opening. Data are from the locations indicated in Fig. 1C. Water levels, waves and currents were recorded over a winter lunar cycle (2 February to 11 March 2014) with winter storm fronts (Nortes). A) Plot of water levels at lagoon ADPC showing daily mixed and tidal cycle (spring tides to neap tides) fluctuations. B) Plot of lagoon and upper shoreface significant wave height (H_s). Note that the largest waves are associated with Nortes, especially on the shoreface. C) Plot of current speed, lagoon and shoreface sensors. D) Rose diagram of H_s direction, magnitude, and frequency in the shoreface. Note that the largest waves come from the northwest; these occur during Nortes. E) Rose diagram of H_s direction, magnitude, and frequency, lagoon data. Data show most of the waves here are from the east, aligning with trade winds. F) Rose diagram of upper shoreface current direction, magnitude, and frequency. The flow to the west-southwest reflects the southwesterly longshore current. G) Rose diagram showing current direction, magnitude, and frequency, lagoon location. The bi-directional currents reflect tidal influence.

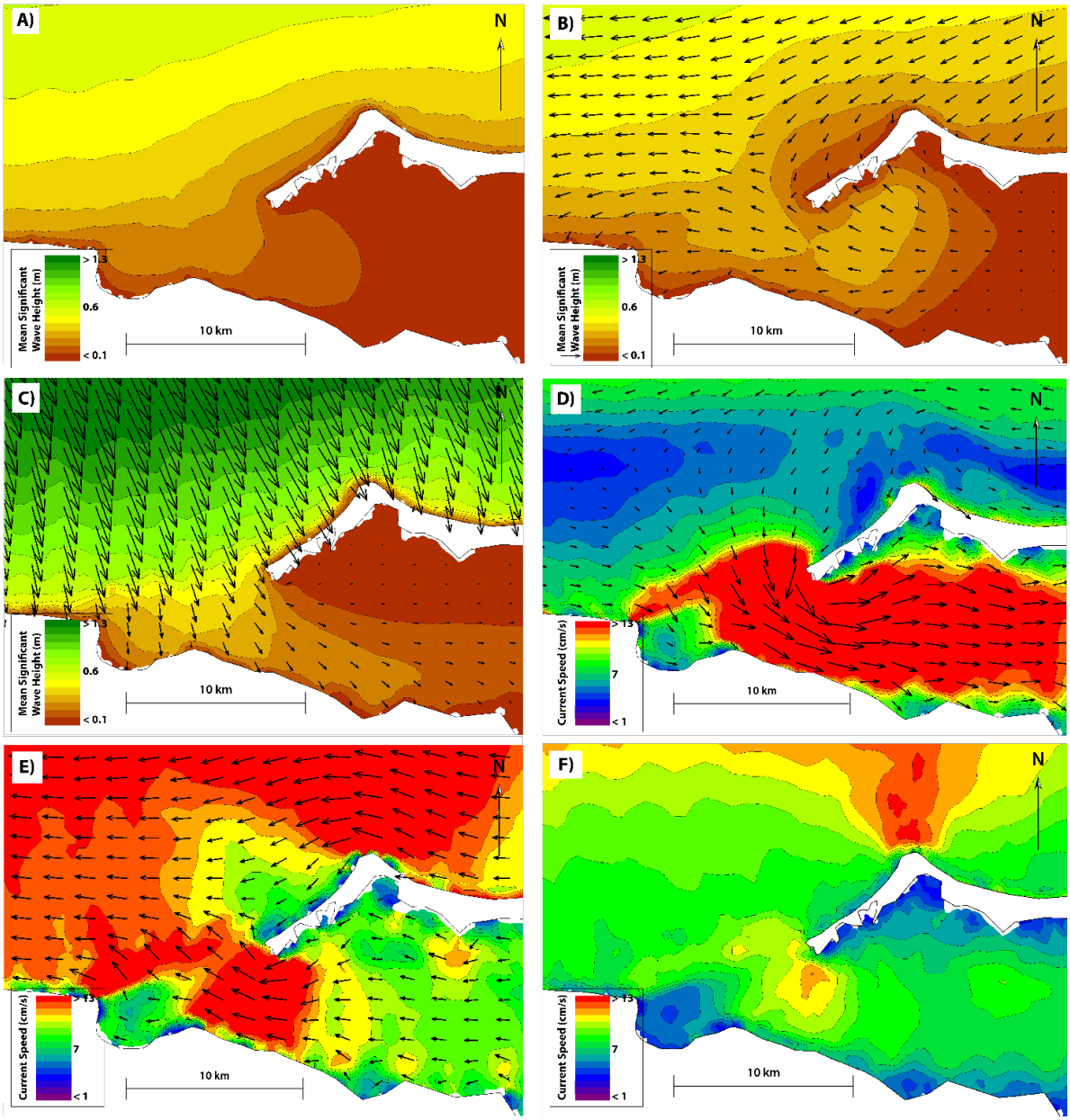

Fig. 10. Wave and current 'base-case' hydrodynamic simulation results. These models approximate physical oceanographic conditions from 2 February to 11 March 2014, the same period data illustrated in Fig. 7. A) Plot of average H_s. Note that the largest average waves are located offshore, in deeper waters. B) Plot of wave directions during easterly trade winds (20 February 2014 2 am). Note most waves are from the east, except along the Isla de Holbox shoreface. C) Plot of wave directions during a representative Norte (13 February 2014 at 1 pm). Note that highest waves occur during Nortes from the northwest direction. D) Plot of current velocities during flood (incoming) tide (13 February 2014). E) Plot of current velocities during ebb (outgoing) tide (19 February 2014). Note by comparing D and E that currents are bi-directional, flowing to the west during ebb tides and to the southeast and east during flood tides. F) Plot of average current speed 2 February to 11 March 2014. Note the strongest currents are located north of the promontory, along the shoreface near the opening, and the western lagoon.

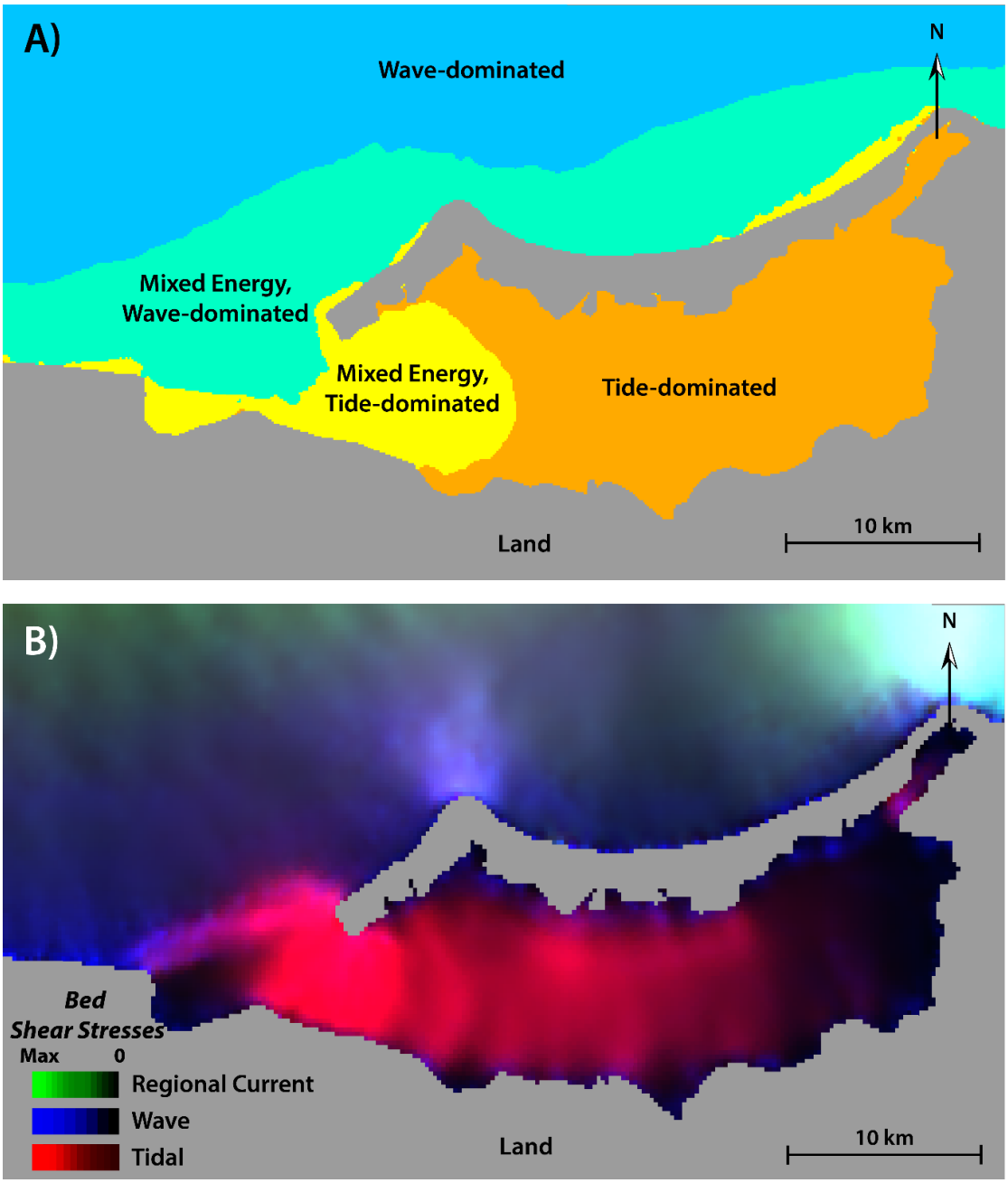

Fig. 11. Hydrodynamic characterization of the study area. A) Delineation of wave-dominated, mixed energy (wave or tide-dominated), and tide-dominated hydrodynamic energy regimes, using method of Hayes (1979). B) Visualization of intensity of different type of bed shear stresses derived from component FM simulations. In this plot, magnitude of bed stress from each component is mapped to a color band (red, green, blue), then the bands are merged into an RGB image. As such, intensity is proportional to bed shear stress, and the colors reflect the dominant controls. The results quantitatively show that the strongest combined bed shear stresses which occur in the western lagoon are dominantly tidal (intense red hue). In contrast, the subaqueous dune fields at the opening of the lagoon are mixed energy (tidal red + wave blue = purple), and the promontories along Isla de Holbox include a mix (elevated wave + regional current + tidal = more saturated white).

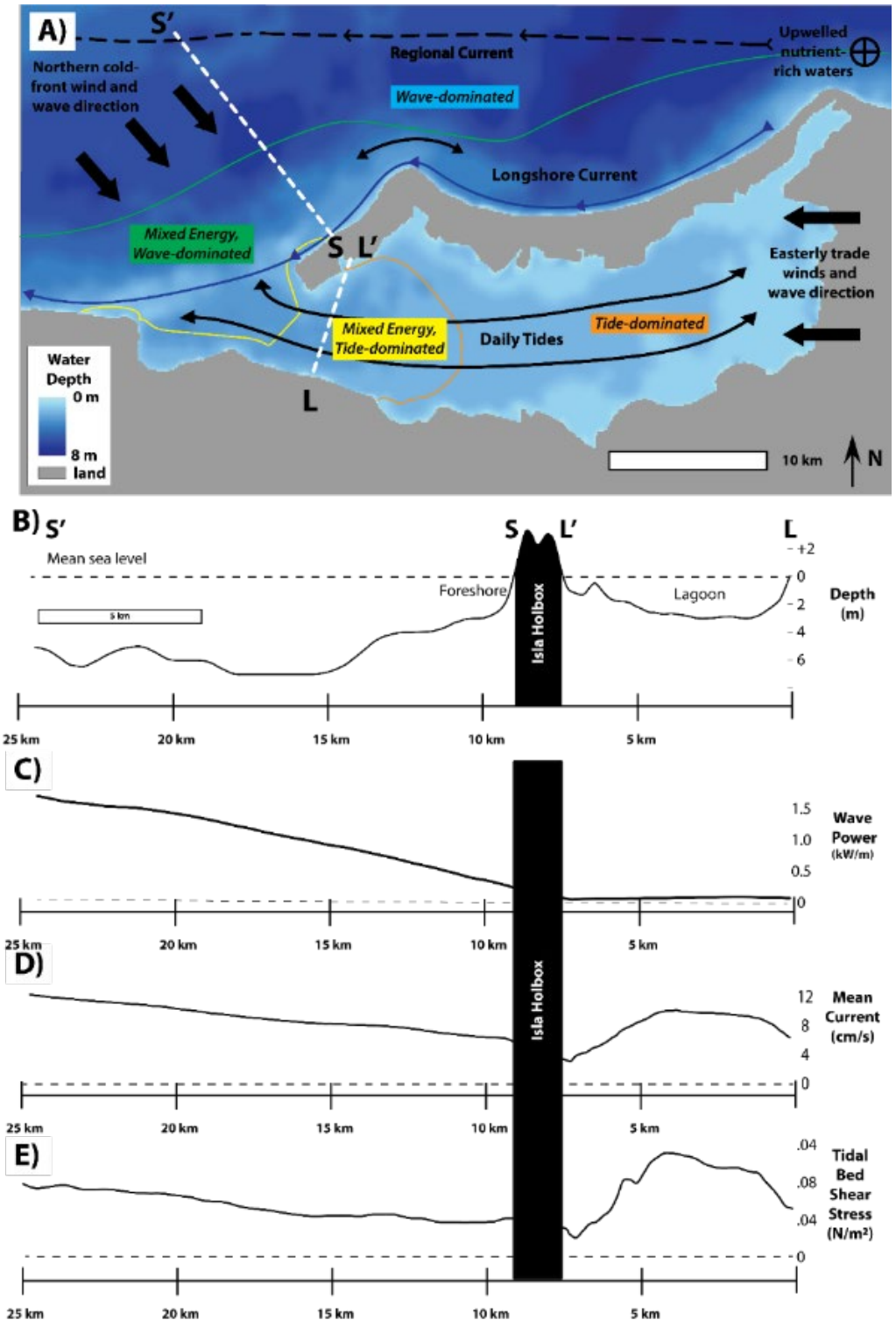

Fig. 12. Generalized conceptual model showing the physical oceanographic processes impacting the high-energy northeastern Yucatán ramp depositional system. A) Schematic summary of the processes. White dashed lines (L-L', S-S') demark the cross-section profiles of depth (B), mean wave power (C), mean current (D) which captures regional current, wave and tidal energy, and E) the tidal energy contribution to bed shear stresses. See text for detailed discussion.

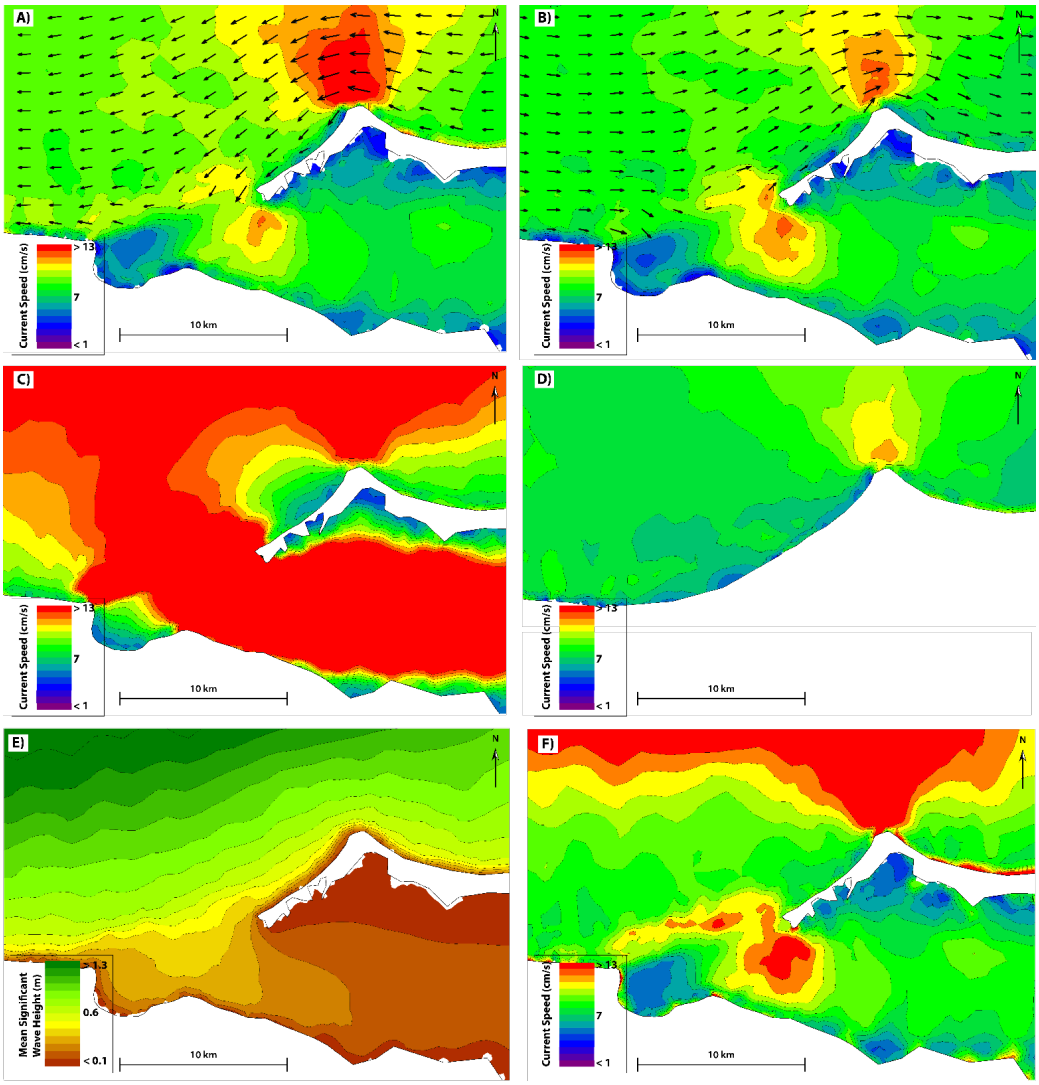

Fig. 13. Conceptual ramp hydrodynamic simulations (cf. Table 2), assessing the impact of a range of variables. Note mean current speed and mean H_s color bars use the same scale as base-case example (Fig. 8). A) Plot of mean current speed of east wind and wave simulation (Table 2, H) with current direction vectors for shoreface areas only (lagoon currents are bi-directional). Data suggest that stronger winds and larger waves from the east result in currents that flow in the same direction with slightly stronger (by 2 to 4 cm/s) velocities, compared to the base-case. B) Plot of mean current speed of west wind and wave simulation (Table 2, I) with current direction vectors for shoreface areas only (lagoon currents are bi-directional). Simulations indicate that stronger winds and waves from the west weakens the current and it also reverses the direction on the shoreface. C) Plot of mean current speed of mesotidal range simulation (Table 2, N). Note that higher tidal ranges facilitate markedly stronger currents, up 25 cm/s greater than the base-case. D) Plot of mean current speed of simulation with lagoon removed (Table 2, O). Without a large lagoon, shoreface mean currents are weaker (by 1 to 10 cm/s) than the base-case. E-F) Plot of Hurricane Wilma (2005) simulation (Table 2, P) of mean H_s (E) and mean current speed (F). During high-intensity, low-frequency tropical storms, relative to the base-case, offshore wave H_s (E) are 0.2 to 0.7 m larger and mean current speeds (F) are 2 to 5 cm/s stronger.

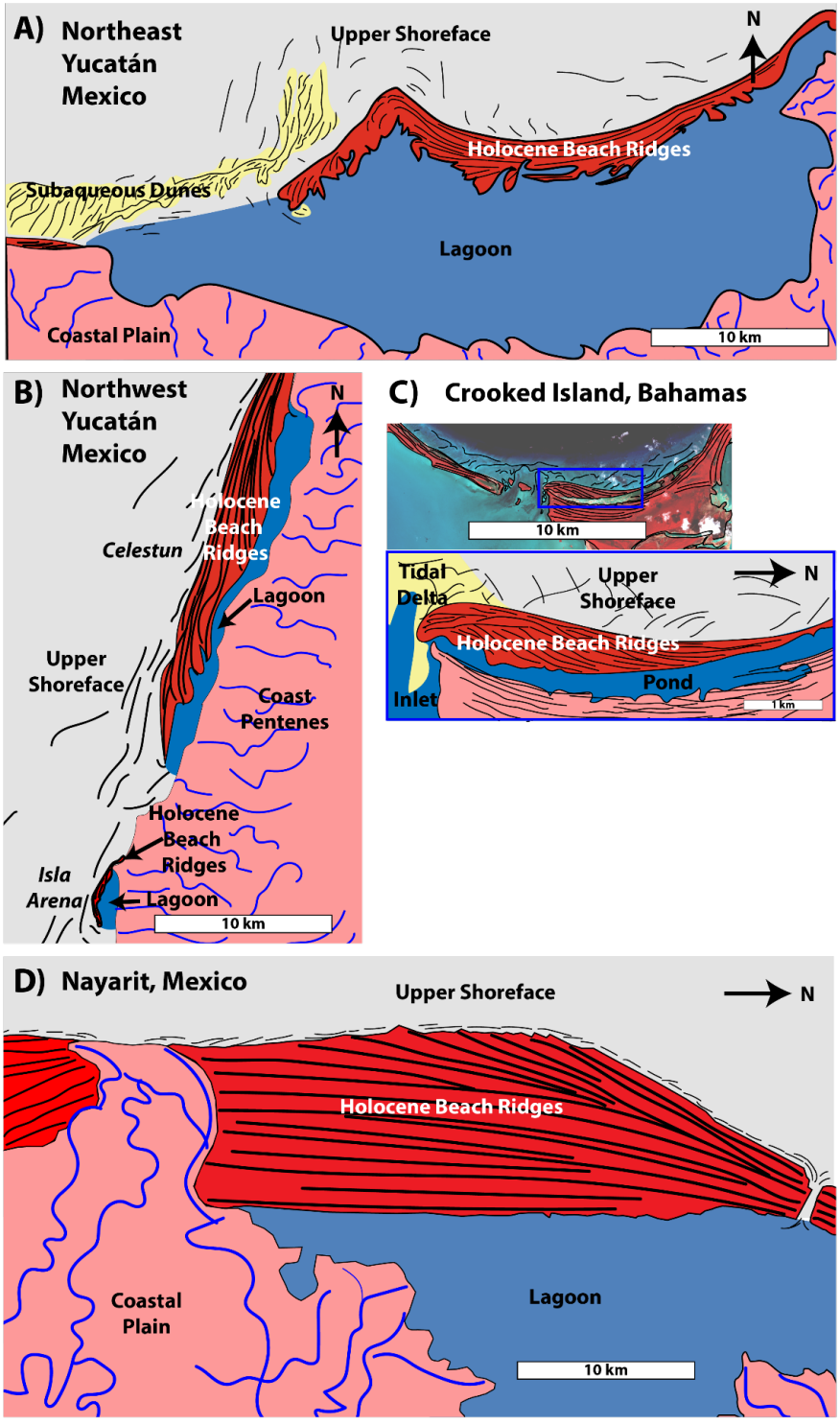

Fig. 14. Comparison of geomorphology of several shoreface systems, plotted at the same scale (except part C, a zoom). Beach ridges denoted by red color, upper shoreface denoted by gray color, subaqueous dunes and bar forms denoted by yellow color. A) Northeastern Yucatán, Mexico. B) Northwestern Yucatán, Mexico (modified from Lowery and Rankey 2017). C) Crooked Island, southern Bahamas (modified from Rankey 2014). D) Nayarit, Mexico (Derived from Plint 2010, Cisneros 2011).

Tables

Module Description	Inputs	Model Parameters	Outputs
MIKE Zero Flexible Mesh generator – creates high-resolution bathymetric meshes	- Water depths and land elevations (from bathymetric survey) - Bounding area	- Mesh sizes – *multiple zones* - Shoreline - *dry land boundaries*	- Bathymetric mesh of 6,669 triangular shaped cells (475 to 1,000 m^2)
MIKE 21 Spectral Wave (SW) – simulates wind-generated waves and swell	- Bathymetric mesh - Wind and wave conditions at northern boundary (hindcast data) - Current (regional)	- Spectral wave equations – *fully spectral formulation* - Spectral discretization – *logarithmic, 360 degrees (10° spacing)* - White-capping – *constant value 6* - Bottom friction dissipation - *Nikuradse roughness, constant 0.009 m* - Wave breaking – *specified gamma, constant 0.8* - Boundary conditions – North: *waves varying time, constant along line*	- Wave radiation stresses (x, y and z) - Significant wave height (H_s) - Maximum wave height (H_{Max}) - Wave period (peak, mean and zero-crossing) - Wave direction (peak and mean), - Wave power (x, y and total - Particle velocities (like orbital wave velocities).
MIKE 21 Flow Model (FM), Hydrodynamic Module - simulates water levels, currents and bottom shear stresses	- Bathymetric mesh - Wave radiation stresses (x, y and z) - Wind conditions (hindcast data) - Water levels (global tide database) - Current (regional)	- Solution technique – shallow water equation – *Higher order, critical CFL number 0.8* - Eddy viscosity – *Smagorinsky formulation, constant 0.28* - Bed resistance – *Manning number, constant 30 ($m^{1/3}/s$)* - Boundary Conditions: West: *water levels varying time and along boundary,* North: *constant flux*, East: *velocities constant u-vel -0.25 m/s*	- Current speed (U and V) - Current direction - Water flux (P and Q) - Bed shear stresses - Surface elevation - Still water depth - Total water depth

Table 1. Hydrodynamic modeling software modules run by DHI MIKE with detailed input, key model parameters, and output parameters. The purpose of these modules is to create a bathymetric flexible mesh of the bottom depths, calculate wind- and swell-generated waves, and estimate flow velocities and water levels based on regional current, wave, wind, and tidal forces. Key model parameters variables selected are denoted by italics. These modules formed the basis of the simulations listed in Table 2.

Simulation	Wind	Wave	Tides	Regional Current
A) Base-Case (existing conditions)	Variable direction and velocity	Variable direction and height	Existing conditions	Southwesterly direction and constant velocity
B) Tide Only	None	None	Existing conditions	None
C) Wind, Wave and Regional Current	Variable direction and velocity	Variable direction and height	None	Southwesterly direction and constant velocity
D) Regional Current Only	None	None	None	Southwesterly direction and constant velocity
E) Wind, Wave and Tides	Variable direction and velocity	Variable direction and height	Existing conditions	None
F) Wind and Wave	Variable direction and velocity	Variable direction and height	None	None
G) Tide and Regional Current	None	None	Existing conditions	Southwesterly direction and constant velocity
H) East Wind and East Waves	Constant 081° 7 m/s	Constant 091° 2 m H_s	Existing conditions	None
I) West Wind and West Waves	Constant 271° 7 m/s	Constant 271° 2 m H_s	Existing conditions	Southwesterly direction and constant velocity
J) South Wind and North Waves	Constant 180° 7 m/s	Constant 000° 0.5 m H_s	Existing conditions	Southwesterly direction and constant velocity
K) Reversed Regional Current	Variable direction and speed	Variable direction and height	Existing conditions	Northeasterly direction and constant velocity
L) Reduced Wind and Waves	Variable direction and ½ speed	Variable direction and ½ height	Existing conditions	Southwesterly direction and constant velocity
M) North Wind and North Waves	Constant 000° 7 m/s	Constant 000° 0.5 m H_s	Existing conditions	Southwesterly direction and constant velocity
N) Mesotidal Range	Variable direction and velocity	Variable direction and height	Five times size of existing tidal range	Southwesterly direction and constant velocity
O) Lagoon Removed	Variable direction and velocity	Variable direction and height	Existing conditions	Southwesterly direction and constant velocity
P) Hurricane Wilma (2005)	Variable direction and velocity	Variable direction and height	Existing conditions	Southwesterly direction and constant velocity

Table 2. List of hydrodynamic simulations including A) base-case (with all forces e.g. wind, wave, tides and regional currents), B-G) isolated and combined forces, and H-P) conceptual ramp simulations. See text for discussion of simulations and results.

Area	Bottom Types	Biota	Sedimentary Structures		Sediment Character			Other
			Biological	*Physical*	*Sizes*	*Sorting*	*Type*	
Lagoon	Muddy Gravel Muddy Sand Gravelly Mud Seagrass	*Halimeda* Seagrasses Bivalves High Spired Gastropod Mangrove marsh	Intense bioturbation rhizoliths common (seagrass/mangrove)	Sparse ripples near mouth of lagoon	Gravel to silt/mud (< 63um) Mean - 431 µm (N=28) Silt/Mud fraction 24 to < 1%	Poorly - very poorly	*Halimeda* - 26% Mollusks - 19% Skeletal grains -19%, Mud , silt, and organic material - 17%, Foraminifera, red algae, and diatoms - < 2%	Broken and micro-bored grains common
Foreshore	Sand Aeolian dunes	Supra-tidal areas plants and arthropods	Aeolian dunes have burrows and rhizoliths	Intertidal areas horizontal to slightly dipping (seaward) planar laminated and cross-bedded. Supratidal areas dune beach ridges	Medium to very fine sand Gravel bioclasts Mean - 287 µm (N=14) Silt/Mud fraction << 0.01%	Bi-modal Moderately well in lower intertidal Poorly in upper intertidal and supratidal	Skeletal grains - 40% Mollusks - 19% *Halimeda* - 12% Lithoclasts - 12% Mililoid/Peneropolid Foraminifera - 5% Echinoderm - 3%	Most grains broken, abraded and bored Larger bioclasts (coquina) grains commonly whole and only slightly abraded
Upper Shoreface	Sand Seagrass Rock	*Halimeda* and Mollusk ubiquitous Foraminfera and Echinoderm common Seagrasses common near foreshore in 2-4 m water depths	Moderate bioturbation in sand areas Intense biorturbation in seagrass area	Wave and current ripples pervasive on mobile sub-strates	Gravel to fine sand Mean - 356 µm (N=116) Silt/mud fraction < 1.2%	Moderately well to poorly	Skeletal grains - 38% Mollusks - 25% Lithoclasts - 12% *Halimeda* - 11% Mililoid/Peneropolid Foraminifera - 5% Echinoderm - 3%	Physical greater than biological reworking of sediment Most grains broken, abraded and bored
Subaqueous Dunes	Sand	Mollusk and Echinoderm common Seagrasses common	Slight bioturbation	Dune amplitudes 0.25 to 1.3 m Complex bi-directional wave and current ripples pervasive	Coarse to fine sand with minor gravel sized bioclasts Mean - 331 µm (N=42) Silt/mud fraction << 1%	Moderately well	Similar to upper shoreface type and abundance	Most all grains extensively broken, abraded and bored

Table 3. Sedimentologic characteristics, bottom types, and biota of each geomorphic element in the Isla de Holbox area.

		Geomorphic Parameter		Hydrodynamic Parameter			
		Distance from Shoreline	*Depth*	*Mean Wave Ht (H_s)*	*Mean Wave Power*	*Mean Current Speed*	*Mean Bottom Shear Stress*
Granulometric Characteristic	*Mean Grain Size*	- 0.017	+ 0.042	+ 0.030	+ 0.064	+ 0.045	+ 0.009
	Sorting (Φ)	***- 0.462***	***- 0.196***	***- 0.236***	***- 0 .190***	- 0.021	+ 0.016
	Silt/Mud %	***- 0.466***	***- 0.201***	***- 0.305***	***- 0.268***	- 0.057	+ 0.021
Grain Type Relative Abundance	*Skeletal Fragments*	***+ 0.431***	+ 0.075	+ 0.194	+ 0.157	- 0.080	- 0.116
	Lithoclasts	+ 0.249	+ 0.142	***+ 0.211***	+ 0.182	+ 0.174	+ 0.085
	Mollusks	***+ 0.301***	***+ 0.348***	***+ 0.378***	***+ 0.376***	***+ 0.217***	+ 0.042
	Foraminifera	***+ 0.346***	+ 0.260	***+ 0.298***	***+ 0.233***	- 0.014	- 0.079
	Echinoids	+ 0.113	+ 0.073	+ 0.163	+ 0.083	+ 0.164	***+ 0.204***
	Halimeda	***- 0.501***	***- 0.224***	***- 0.408***	***- 0.328***	- 0.088	+ 0.048
Bottom Type Percentage	*Sand Bottom*	***+ 0.240***	+ 0.049	+ 0.126	***+ 0.159***	- 0.033	- 0.138
	Seagrasss Bottom	+ 0.159	- 0.150	+ 0.214	+ 0.136	+ 0.208	+ 0.188
	Rock Bottom	- 0.039	+ 0.252	+ 0.036	- 0.079	- 0.125	- 0.075

Table 4. Statistical relations between geomorphic - hydrodynamic parameters and granulometric - grain type – bottom type characteristics. Data are illustrated as pairwise correlations (r) between two variables. Red color indicates negative correlations and black color positive correlations. Statistically significant relationships (P values < .05) demarked by bold italicized text.

Predicted Characteristic	R^2 Value	P Value	Highest Contributing Geomorphic and Hydrodynamic Parameters*			
			First	Second	Third	Fourth
Mean Grain Size	0.04	0.7170	Depth	Mean Wave Direction	Distance from Shoreline	Mean Wave Power
Sorting (Φ)	0.27	<0.0001	Distance from Shoreline	Depth	Mean Current Speed	Mean Bottom Shear Stress
Silt/Mud %	0.26	<0.0001	Distance from Shoreline	Depth	Mean Wave Direction	Mean Current Speed
Skeletal Fragments	0.42	<0.0001	Depth	Peak Wave Period	Mean Wave Direction	Distance from Shoreline
Lithoclasts	0.29	0.0006	Peak Wave Period	Mean Wave Power	Mean Current Speed	Mean Bottom Shear Stress
Mollusks	0.27	0.0037	Mean Current Direction	Depth	Mean Current Speed	Mean Wave Height
Foraminifera	0.22	0.0151	Mean Wave Direction	Distance from Shoreline	Peak Wave Period	Depth
Echinoids	0.15	0.2189	Mean Wave Power	Mean Wave Height	Mean Current Speed	Distance from Shoreline
Halimeda	0.43	<0.0001	Peak Wave Period	Distance from Shoreline	Mean Current Direction	Depth
Sand Bottom %	0.24	<0.0001	Depth	Distance from Shoreline	Peak Wave Period	Mean Current Speed
Seagrass Bottom %	0.23	0.2288	Depth	Mean Wave Direction	Distance from Shoreline	Mean Current Direction
Rock Bottom %	0.27	0.1577	Distance from Shoreline	Mean Wave Height	Mean Wave Power	Mean Wave Direction

* Multiple linear regression model input parameters: depth, distance from shoreline, mean wave height, peak wave period, mean wave direction, bed horizonal particle velocity, mean wave power, mean water flux, mean current speed, mean current direction, and mean bottom shear stress

Table 5. Multiple linear regression modeling data showing the statistical relations between 11 geomorphic - hydrodynamic parameters (listed at bottom of table) and each granulometric - grain type – bottom type characteristic. R^2 and P values are listed for each predicted characteristic model as well as the highest four contributing parameters. The data indicate that sorting, abundance of sediment < 125 µm, unidentified skeletal fragments, lithoclasts, mollusks, *Halimeda*, and rock and mud bottom types are influenced by geomorphic and hydrodynamic parameters.

Wave Height

Area

Conceptual Ramp Simulation	Lagoon	Opening	Foreshore	Shoreface	Punta Laguna
H. East Wind and Wave	+ 50 % to 2.5 x	+ 15 %	- 35 %	- 5 to 35 %	+ 10 %
I. West Wind and Wave	+ 50 % to 10 x	+ 40 %	+ 30 %	+ 5 to 20 %	- 15 % east of promontory
M. North Wind and Wave	- 50 %	+ 50 %	+ 100 %	+ 70 to 80 %	+ 80 %
J. South Wind and North Wave	- 50 to 75 %	- 40 %	- 15 %	- 30 to 40 %	- 30 %
L. Reduced Wind and Wave	- 60 to 80 %	- 55 %	- 40 %	- 45 to 55 %	- 45 %
K. Reversed Regional Current	same	same	same	same	same
N. Mesotidal Range	same	same	same	same	same
O. Lagoon Removed	N/A	- 30 %	- 15 %	- 3 to 5 %	- 3 %
P. Hurricane	+ 50 % to 5x	+ 50 %	+ 50 to 90 %	+ 100 %	+ 60 %

Current Speed

Area

Conceptual Ramp Simulation	Lagoon	Opening	Foreshore	Shoreface	Punta Laguna
H. East Wind and Wave	± 2 %	± 5 %	+ 15 %	+ 5 to 25 %	+ 15 %
I. West Wind and Wave	± 5 %	- 5 to 10 %	+ 15 % direction reversed	± 10 % direction reversed	- 15 % direction reversed
M. North Wind and Wave	± 5 %	± 10 %	+ 20 to 35 %	- 10 to 35 %	- 35 %
J. South Wind and North Wave	± 5 %	± 5 %	- 50 %	- 30 to 50 %	- 55 %
L. Reduced Wind and Wave	± 10 %	± 5 %	- 50 %	- 25 to 55 %	- 45 %
K. Reversed Regional Current	± 7 %	+ 5 %	- 5 to 10 %	- 5 to 25 %	- 15 %
N. Mesotidal Range	+ 1.5 to 2.0 x	+ 2.25 x	- 5 to 20 %	+ 20 to 75 %	+ 10 %
O. Lagoon Removed	N/A	- 25 to 50 %	- 10 to 30 %	- 10 to 50 %	- 10 %
P. Hurricane	+ 50 %	+ 35 %	+ 30 to 55 %	+ 10 to 40 %	+ 20 %

Table 6. Comparison of results of conceptual ramp simulations with base-case simulation (existing conditions). Results are expressed in terms of relative change in mean wave height and current speed. In this table, red color means greater than and black color reflect less than base-case values.

	Carbonate	Siliciclastic
Sediment Source and Climate	Sediment production *in situ*	Sediment sourced from older rocks, generally from distant locations
	Climate strong control on sediment production (e.g., seawater temperature)	Climate generally indirect influence (e.g., nature of weathering, vegetation, influence on sediment transport)
Physical and Chemical Processes	Ocean chemistry and circulation (e.g., upwelling and elevated nutrient levels) important control on sediment association	Ocean chemistry and circulation minor influence
	Physical properties (e.g. waves, tides, and currents) not dominant influence on sediment production and character	Physical processes primary, if not sole, control on sediment character
	Sediment commonly cemented	Sediment remains unconsolidated in depositional environment
	Wind direction relative to shoreline can impact upwelling and nearshore nutrient levels	Wind direction, upwelling, and nutrient levels insignificant control
	Windward vs. leeward differences on sediment production and resultant geomorphology	Wave, tide, and/or fluvial power differences on sediment transport, deposition, and geomorphology
	Focused tidal or wave energy enhance sand body development	Focused tidal or wave energy enhance sand body development
Geomorphology	Coastal dune, sandy foreshore and upper shoreface, subaqueous dunes, barrier islands, and protected lagoons	Grossly similar geomorphic elements
	Physical sedimentary structures and bedforms include foreshore, seaward-dipping, laminated units, upper shoreface trough cross beds, and subaqueous dunes	Similar physical sedimentary structures and bedforms
	Variety of spatial scales (10-100 m to + 100 km)	Variety of spatial scales (1-100 m to + 100 km)
Granulometry	Sediment type based on biota	Sediment type based on source rock
	Grain size reflects size of skeletons	Grain size reflects source rock, transport path, and hydraulic energy of deposition
	Sorting reflects *in situ* production and hydraulic energy of deposition	Sorting reflect hydraulic energy of deposition
	High-energy shorefaces lack mud	High-energy shorefaces lack mud
	Mud abundance is basis for classification method of carbonates	Mud abundance reflects hydraulic energy of deposition

Table 7. Comparison of carbonate and siliciclastic wave-dominated shorefaces (derived from Dalrymple 2010 and James 2010).

Appendices

Appendix I – Comparison with Other Heterozoan Shelves

The sedimentology, geomorphology, and oceanographic processes of the northeastern Yucatán ramp have some striking similarities but also exhibit marked differences with other heterozoan shelf systems. Comparison between this system (and the conceptual ramps) with other Holocene heterozoan shelves provides greater insight into the influence of chemical and physical processes on the sedimentary characteristics and patterns of carbonate sediment deposition of ramp systems.

Northwestern part of the Yucatán Shelf, Mexico. – Although they are part of the same system, the northwestern part of the Yucatán Shelf has several oceanographic, geomorphic, and sedimentologic differences to the northeastern Yucatán ramp. This side of the Yucatán peninsula, near Celestún and Isla Arena to the south (Fig. 1), includes the same easterly trade winds, but here they blow directly offshore. This area includes gentler shoreface gradient, shallower water, and smaller lagoons (Lowery and Rankey 2017).

Despite being open to the westerly and northwesterly Norte storms, the Yucatán Peninsula shields this region from the prevailing easterly trade winds and strong easterly tropical storms resulting in lower overall wave energy levels. In this context, the conceptual simulations of reduced wind and wave along with the south wind with north wind simulation (Tables 2 and 6, simulations L, J) most closely align with the northwestern Yucatán conditions. These simulations demonstrate lower energy in the shoreface, consistent with the observations of more mud prone, less sorted sediment, and reduced abrasion located in this area. The shoreface has shore-parallel belts of mollusk- and *Halimeda*-rich muddy sands and gravels with increasing fines at depth (Lowery and Rankey 2017). In the lagoon, *Halimeda* is scarce, mud averages 39% abundance,

and organic material is much more abundant. Additionally, in neither the shoreface nor the lagoon are rocky bottoms exposed, perhaps due to the less pronounced sweeping, and therefore lithoclasts are absent. Overall, the northwestern Yucatán Shelf is a lower energy muddy ramp system.

The two systems nonetheless share some similarities. First, they are on the Yucatán Shelf and both lack siliciclastic influx (Logan 1969). Second, they are both impacted by the same climate, have similar tidal range, and encounter cool, nutrient-rich upwelled waters (Enriquez et al. 2010, Ruiz-Castillo et al. 2016). Third, although grain size distribution and relative abundance of different grain types vary between the shelves off the northeastern and northwestern peninsula, the sediment across both areas is predominately heterozoan, and composed mainly of molluscan and *Halimeda* skeletal grains. Most of the photozoan assemblage is suppressed, and warm-water scleractinian corals are not found in either area, despite the shallow water. Overall, this comparison illustrates that although the westward drift of cooler, upwelled water facilitates a similar floral and faunal assemblage, the different orientations and thus energy level create distinct bottom type associations and granulometric characteristics.

South Australia Shelf – The largest modern cool-water carbonate system in the world, the South Australia Shelf is an immense, wide and relatively flat submarine plain that is over 1,500 km long, ranging from 80 to 260 km wide, with depths up to 120 m (James 1997). The shelf differs from the Yucatán Shelf in several ways. First, the climate is arid sub-tropical to temperate with southeast summer and westerly winter winds and seasonal currents. Second, the Southern Ocean has some of the largest waves in the world (mean annual 2.5 m H_s), and, as a result, this shelf is a storm-dominated system, with southwesterly waves directly approaching the coastline (James et al. 2001, Bourman et al. 2016). Third, the shelf has a semi-diurnal tidal regime with mesotidal range up to 1.3 m during spring tides. Finally, downwelling is prevalent across the shelf with

common relatively low nutrient waters, except in the eastern areas during localized summer coastal upwelling (James et al. 2001, Kampf et al. 2003).

This ramp system has higher wave and tidal energy than the Yucatán. The north wind and wave and the mesotidal conceptual ramp simulations (Table 2 and 6, simulations M, N), with high winds and waves striking perpendicular to the coastline with a mesotidal range, mimics some nearshore conditions on the South Australia Shelf. These simulations illustrate greater orbital velocities and bottom currents, which would be expected to favor accumulation of coarser grains or winnowing and non-deposition.

Surficial sediments of the South Australia Shelf are a mixture of lithoclasts and Holocene skeletal fragments (James et al. 2001). Sediments are a mixture of sand, gravel and cobble sized grains. Nearshore or inner shelf sediment includes abundant red algal, mollusc, and benthic foraminifera fragments. Further offshore, on the middle and outer shelf, sediment is composed mainly of lithoclasts and bryozoans.

Despite these differences, the two systems include several similarities. Both are large, broad, relatively shallow shelf systems with shoreface parallel to the general wind direction. Terrigenous sediment influx onto the South Australian shelf is also minimal with most sediment being carbonate, and produced on the shelf (James et al. 2001, Bourman et al. 2016). Although South Australia has a diversity of coastal landscapes including extensive coastal cliffs, there are expansive barrier island systems, with aeolian dunes, and back-barrier lagoons along the coastline (Bourman et al. 2016). In the nearshore more protected areas, seagrasses are abundant and mangroves are common in the intertidal and supratidal area of the lagoons and gulfs. The inner and middle shelf areas have relatively thin veneers of surficial sediment or exposed rocky bottoms.

Most all the sediment is entirely heterozoan association carbonate grains either from modern skeletal fragments or lithoclasts (James et al. 2001).

Mauritania Shelf, West Africa -- The shelf off northern Mauritania, West Africa, has several differences in the processes, geomorphology, and sediments compared to the northeastern part of the Yucatán ramp. This shallow and broad (up to 160 km) shelf open to the Atlantic Ocean has a flat-topped depositional profile in the north that transitions to a narrower homoclimal ramp to the south (Klicpera et al. 2015). It has an arid tropical climate and is bounded by Sahara Desert (Vermeer 2010), equatorial trade winds blow siliciclastic sediment off the desert onto the shelf, creating a mixed carbonate and siliciclastic system (Michel et al. 2011). Coarse sand deposited along the shoreline is driven southward by longshore drift, and mixed with aeolian silt that is deposited across the shelf (Vermeer 2010). As a result, siliciclastics are abundant in the intertidal zone, along the shoreline, inside the protected lagoon, and the southern shelf areas (due to the southward sediment transport) (Klicpera et al. 2015). Cool, upwelled, nutrient-rich water from the southward-flowing Canary Current mixes with warm, northward-flowing Guinea Current water on the shelf, resulting in seasonal fluctuations in water temperature, salinity, and nutrient level (Michel et al. 2011, Klicpera et al. 2015). Both upwelled water and aeolian silt fertilize the water, resulting in Chl-*a* values 3 to > 10 mg m^{-3}, making it one of the most productive marine areas in the world (Michel et al. 2011, Klicpera et al. 2015). Ooids are rare and only found in the enclosed lagoons along the shoreline and peloids are common within shallow inner and the deeper open shelf regions (Klicpera et al. 2015).

The Mauritania and the Yucatán shelves are both in the tropics in the trade wind belt. Open to the Atlantic Ocean, the Mauritania shelf is impacted by a mix of ocean swells from the northwest, wind waves, tides, and wind-driven and deep currents (Michel et al. 2011). The tidal

range is microtidal (< 1 m) with stronger tidal currents inshore, near embayments, and inside the tidal channels of shallow bank (Vermeer 2010, Michel et al. 2011). These physical oceanographic conditions resemble those of the northeastern Yucatán ramp. The base-case simulation (Table 2 and 6, simulation A), a high-energy wave-dominated system, most closely resembles the physical conditions on Mauritania Shelf.

With the somewhat comparable chemical and physical oceanographic conditions, there are several sedimentological similarities. The Mauritania Shelf is dominated by heterozoan association carbonate skeletal grains (primarily mollusks) along with relict lithoclasts, despite the tropical location (Michel et al. 2011, Klicpera et al. 2015). Typical tropical warm water photozoan carbonate producers such as hermatypic corals, calcareous green algae, and large benthic foraminifera are absent (Michel et al. 2011). Hydrodynamics generally controls the grain size distribution and sorting of both carbonates and siliciclastic sediment, and similar bioclastic composition across the shelf (Michel et al. 2011). In this high-energy system, sediment is abraded and fragmented leading to large proportions of undeterminable skeletal fragments (Michel et al. 2011). Finer grained sediment is mostly winnowed and transported off the shelf with higher silt/mud and fine sand deposited in the more protected nearshore and southern shelf areas (Michel et al. 2011, Klicpera et al. 2015).

Synthesis – These systems have differing nutrient levels. The Mauritania shelf has the highest nutrient levels (eutrophic conditions) of these systems, with strong upwelling conditions, and has primarily heterozoan-dominant carbonate sediments mixed with some fine aeolian siliciclastics. Both nearshore systems along the Yucatán Shelf have upwelling conditions, nutrient levels that are 3 to 10 times less than those of Mauritania Shelf and has a mixed heterozoan and photozoan grain association. Compared to the other locations, the nutrient levels on the South

Australia Shelf are relatively low, with downwelling conditions present, except for some areas with localized coastal upwelling. Despite lower nutrient levels, the South Australia Shelf has heterozoan-dominant grain association, likely due to the cooler seawater temperatures found in its sub-tropical to temperate regions. These results illustrate the concept that the level of nutrients (as associated with intensity of upwelling) and seawater temperature controls whether the heterozoan, mixed heterozoan-photozoan, or photozoan assemblage is present (Hallock and Schlager 1986, James 1997, Pomar et al. 2004, Westphal et al. 2010, Michel et al. 2011, Klicpera et al. 2015).

In addition to differences in nutrient levels, these Holocene systems also have different wave conditions which in turn also influence the character of the sediment. Protected from the persistent easterly trade winds and waves, the northwestern Yucatán Shelf nearshore region has the lowest wave energy. Here, rocky bottoms are absent; the bottom is sediment- or vegetation-covered, *Halimeda* is common, and lithoclasts are rare. The shore-parallel bottom-type zones include increasing fines with increasing depth, and grains are less abraded and remain unbroken. Despite these differences, beach ridges are similar in structure and extent in both Yucatán systems (Fig. 12), although the northwestern Yucatán Shelf beach ridges composition have larger skeletal fragments and coquina. In higher wave energy systems such as the northeastern Yucatán ramp and the Mauritania Shelf, the sediment lacks mud, the skeletal grains are more frequently broken, and abraded; exposed rocky bottoms are common, and are associated with lithoclasts. Finally, the South Australia Shelf has the highest wave energy of these systems. As a result, the bottom is scoured of most surficial sediment, and fines are transported off-shelf; grains remaining on the shelf are coarse skeletal fragments and relict lithoclasts. For all three high-energy systems, waves move and suspend sediment and then currents transport the fines off the shelves (James et al. 2001, Michel et al. 2011, Klicpera et al. 2015). These comparisons reveal how the level and direction of

wave energy influences the sediment, with higher wave energy commonly reflected in rocky bottoms with abundant relict grains, but overall sediment is grainier, broken, and abraded.

Despite microtidal ranges in all but South Australia, the tidal forces are dominant in the wave-protected lagoons and embayments of these systems. The high wave energy from the open shelf is dissipated by either the sheltering barrier islands or fringing island/reefs. Inside the lagoons and embayments of the Yucatán and South Australian shelves, the sediment generally is composed of muddy sand and muddy gravel, with seagrasses and mangroves common. In contrast, the nearshore areas of the Mauritania Shelf are dominated by siliciclastics. Lagoon sediments are mostly fine-grained, but focused tidal energy can impact sediment transport and deposition. For example, the highest currents in the northeastern Yucatán system are within the lagoon tidal channels covered by coarse sand and gravel. Tidal forces can couple with wave energy near the mouth of lagoons and embayments, favoring occurrence of bars or subaqueous dunes. In the Yucatán, for example, a sandy bar forms south of the mouth of smaller Isla Arena lagoon (Figs. 1A and 12B) with an expansive bar and subaqueous dune fields forms at the opening of the larger Laguna de Yalahau (Fig. 1C). Although these systems are generally wave-dominated, the impact of tidal energy is pervasive, and contributes the heterogeneity of the sediment, especially in nearshore areas.

Appendix II – Comparison with other Wave-dominated Shoreface Systems

Whereas appendix I compared heterozoan shelf systems with similar chemical as well as physical oceanographic conditions, comparisons with other wave-dominated shoreface systems (e.g., photozoan-dominated carbonates and siliciclastic) provides insight into the primary influence of physical processes on sediment character and geomorphology of wave-dominated shoreface systems.

Western Shelf of Crooked-Acklins Platform, southern Bahamas –The Crooked-Acklins platform, a large (ca, 2,600 km^2) bank in the Southern Bahamas, includes a photozoan, wave-dominated shelf west of Crooked Island and Long Cay. This region, has a tropical semi-arid climate, has a tidal range of < 1 m (microtidal), lies on the leeward margin of the Crooked-Acklins platform, with no upwelling or influx of nutrient-rich waters, and is occasionally beset by hurricanes. The west-facing shelf is 2 km wide, and consists of an arcuate beach ridge - sandy shoreface complex (Fig. 12C) that drops abruptly into the basinal Crooked Island Passage. The system is low energy - most waves are 0.1 m H_s, maximum waves reach 0.3 m, and currents generally weak (<10 cm/s), with a net southerly flow (Rankey 2014).

Series of low Holocene beach ridges up to 1 km wide line the shoreface and commonly are topped with hard cemented surfaces (beachrock) (Rankey 2014). The foreshore gently dips seaward and consists of low-angle laminated beds of oolitic-peloidal-skeletal moderately well-sorted, fine to medium sand. Upper shoreface sediment consists of moderately sorted medium to coarse sand of ooids, peloids, composite grains, fragments of *Halimeda*, foraminifera, mollusks, and corals and form low-amplitude subaqueous dunes and rippled sand bodies to a depth of 3-4 m (Rankey 2014). An ebb-tidal delta of shallow, mobile fine-medium ooid-peloid-skeletal sand forms at the break between Crooked Island and Long Cay (Rankey 2014). The outer, deeper part

of the shelf includes wave ripples or bioturbated bottom and scattered low relief patch reefs, before passing sharply at a drop-off at *ca* 15 to 25 m water depth into water several hundred meters deep.

Lower Cretaceous, Northern Gulf of Mexico – Carbonate beach successions from high energy wave-dominated settings are scarce in the geologic record. This paucity of ancient beach and nearshore successions may be due to a lack of recognition rather than absence of preservation (Inden and Moore 1983, Kerans and Loucks 2002). Some of the best-known examples of ancient carbonate beach deposits are from the Lower Cretaceous (Aptian-Albian) of the Northern Gulf of Mexico (Inden and Moore 1983). These successions formed on broad ramps or rimmed platforms along the margins of proto-Gulf of Mexico and had a generally humid semi-tropical climate (Scott 1993). Composed primarily of rudstones and grainstones of skeletal fragments, caprinid rudists and oysters, the preserved beach complexes occurred under stable tectonic conditions (Kerans and Loucks 2002, Owen and Kerans 2010). As in the northeastern Yucatán ramp, the sediment of these beach complexes (upper shoreface and foreshore) were deposited under high-energy wave-dominated conditions (Owens and Kerans 2010) and formed similar geomorphic elements and physical sedimentary structures.

During the Lower Cretaceous, the climate was generally humid semitropical (Scott 1993), and tidal ranges were microtidal (Owens and Kerans 2010). These areas were most likely impacted by larger waves generated by persistent trade winds blowing parallel to the shoreface. Trade winds of the Lower Cretaceous Northern Gulf of Mexico would have transported surface waters onshore (by Ekman transport), thereby creating conditions more favorable to downwelling. These areas likely had lower nutrient levels than the modern Yucatán Shelf. As a result, the Lower Cretaceous beach and shoreface areas had more abundant photozoan association carbonate producers, as well

as coated grains. Additionally, terrigenous sediment entered the shoreface via fluvial inputs and was transported along the shoreline (Kerans and Loucks 2002).

Wave-dominated Siliciclastic Shorefaces – Carbonate and siliciclastic sediments commonly are treated as separate and distinct. They have fundamental differences in their composition, sourcing, range of depositional environments, the influence of climate and ocean chemistry, and diagenesis (Dalrymple 2010). Terrigenous clastic sediment is derived from the weathering, erosion and transport of siliciclastic source rocks most often located inland on topographic highs (James 2010). Upon deposition, the patterns of sedimentary texture, structures, and grain size variations are a result of the local hydraulic forces (James et al. 2010). Siliciclastic coastal depositional environments commonly are subdivided by the dominant physical process (fluvial, wave, and tide) (Boyd et al. 1992, Dalrymple 2010).

Specifically, wave-dominated siliciclastic shoreface systems (e.g. Nayarit, Mexico; Gulf Coast Texas, USA) are compared with previously discussed carbonate shorefaces and heterozoan shelf systems. Broadly, wave-dominated shorefaces lie at balance between relative sea level change, rate of sediment supply, and the dispersal processes, primarily by waves (Heward 1981, Davis and Clifton 1987, Clifton 2006). They usually face large shelves open to waves and storms. Progradational beach-ridge complexes with a strandplain of parallel beach ridges (e.g. Nayarit, Mexico) (Fig. 12D) can form during sea-level regression and/or with adequate sediment supply (Davis and Clifton 1987, Boyd et al. 1992). Transgressive barrier islands (e.g. Atlantic and Gulf Coasts, U.S.A.) typically occur with sea level rise or during sea level fall if sediment supply is minimal accompanied by high-energy conditions (Heward 1981, Davis and Clifton 1987). In general, geomorphic elements include sandy high-energy foreshores, upper shorefaces commonly with elongate coast-parallel sand bodies (e.g. sheet sands, tidal deltas, and barrier bars), grading

into sandy middle and lower shorefaces (Clifton 2006, Plint 2010). Foreshore and upper shoreface gradients are strongly influenced by the sediments grain size, coarse-grained gravelly beaches are steep whereas sandy beach slope more gently (Plint 2010). Mostly silicate minerals, grain type is controlled by composition of the source area with weaker grains selectively removed by weathering and during transport (Dalrymple 2010). Grain size and sorting is controlled by composition and relief of source area, hydraulic energy along transport and during deposition (Dalrymple 2010). Despite these differences, comparison between the systems, especially with the physical processes in the shallow marine environment of deposition, are instructive and highlight the common influence of the hydrodynamic forces upon the patterns and variations of the deposited sediment.

Synthesis – Comparisons between these wave-dominated shoreface systems and the modern Yucatán Shelf highlight several differences in processes, geomorphology, and sedimentology. First, contrasting with carbonate shelf systems, the influence of ocean chemistry and circulation (e.g. upwelling and elevated nutrient levels) has only minor influence on siliciclastic wave-dominated shoreface systems (Dalrymple 2010). Second, the role of cementation varies between the systems. For example, Crooked Islands has beach rock that can limit beach erosion and also form composite grains (Rankey 2014). In the northeastern Yucatán Shelf, the bedrock promontory (Punta Mosquito) limits erosion (e.g. rocky bottoms are swept clean of sediment that would otherwise be eroded) and effects the hydrodynamics, geomorphology, and sediment of adjacent areas. Third, most carbonate sediment originates *in situ*, unlike in siliciclastic shoreface systems where sediment is derived from eroding older rocks, and transport to the location of deposition (James 2010). Grain size variations are due mainly to changes in hydraulic forces (James 2010). This contrasts to the northeastern Yucatán ramp where the mean grain size

and grain size abundances > 125 μm did not correlate with hydrodynamics, depth, or distance from shoreline (Tables 4 and 5). Thus, in the carbonate systems, sediment can be deposited that is not in hydrodynamic equilibrium with ambient conditions. Physical processes are the dominate control on siliciclastic sediment deposition, from origin to transport to deposition. In contrast to physical processes are only one of the many controls on carbonates. Fourth, sediment supply and reworking rates differ. The rocky bottom offshore along with more longshore transport than progradation in the northeastern Yucatán ramp suggest perhaps a limited sediment supply with more sediment reworking as compared with the northwestern Yucatán Shelf. This contrasts the abundant sediment supply supporting the extensive prograding siliciclastic beach ridges of Nayarit, Mexico. Finally, each shoreface system has different assemblages of grain types. As mentioned previously, siliciclastic system grains are based on the source area composition. Crooked Island and the Lower Cretaceous of Northern Gulf of Mexico systems are predominately photozoan but with differing sets of carbonate producers (e.g. rudist of Lower Cretaceous). The Yucatán Shelf has mixture of heterozoan (predominately) and photozoan assemblages.

Despite these differences, the shorefaces exhibit some similarities in processes, patterns of deposition, and sedimentary structures. First, the sediment, once formed, is transported in the wave-dominated environment according to the laws of physics. Second, the geomorphic elements are grossly comparable with coastal dune, sandy foreshore and upper shoreface, and longshore transport of sediment forming subaqueous dunes in the shoreface and creating the protected lagoons and barrier islands (Fig. 12). Third, the general sedimentary structures in each environment are similar. Foreshores have gently seaward-dipping, laminated units, upper shorefaces include gently inclined and include numerous sand bodies (e.g. subaqueous dunes, sheet sands, subaqueous dunes), and lagoons are muddy, rich in seagrass, and commonly lined with

mangroves. Finally, except in the lowest-energy system (northwestern Yucatán), these wave-dominated shoreface systems lack of mud within the high-energy shorefaces.

Appendices References

BOYD, R., DALRYMPLE, R., ZAITLIN, B.A., 1992, Classification of clastic coastal depositional environments: Sedimentary Geology, v. 80, p. 139-150.

CLIFTON, H.E., 2006, A reexamination of facies models for clastic shoreline, *in* Posamentier, H.W., and Walker, R.G., eds, Sea-level Fluctuation and Coastal Evolution: Society of Sedimentary Geology Special Publication, v. 84, p 293-337.

DAVIS, R.A., JR., AND CLIFTON, H.E., 1987, Sea-level change and the preservation potential of wave-dominated and tide-dominated coastal sequences, *in* Nummedal, D., Pilkey, O.H., and Heward, J.D., eds, Sea-level Fluctuation and Coastal Evolution: Society of Sedimentary Geology Special Publication, v. 41, p 167-178.

HEWARD, A. P., 1981, A review of wave-dominated clastic shoreline deposits: Earth-Science Review, v. 17, p 223-276.

INDEN, R.F., C.H. MOORE, 1983, Beach environment, *in* Scholle, P.A., Bebout, D.G., and. Moore, C.H., eds., Carbonate depositional environments: American Association of Petroleum Geologists Memoir, v. 33, p. 211-265.

KAMPF, J., DOUBELL, M., GRIFFIN, D., MATTHEWS, F.L., AND WARD, T.M., 2004, Evidence of a large seasonal coastal upwelling systems along the southern shelf of Australia: Geophysical Research Letters, v. 31, p. 1-4.

KERANS, C., AND LOUCKS, R.G., 2002, Stratigraphic setting and controls on occurrence of high-energy carbonate beach deposits: Lower Cretaceous of the Gulf of Mexico: Gulf Coast Association of Geological Societies Transactions, v. 52, p. 517-526.

LOUCKS, R.G., 2002, Controls on reservoir quality in platform-interior limestones around the Gulf of Mexico: Example from the Lower Cretaceous Pearsall Formation in South Texas: Gulf Coast Association of Geological Societies Transactions, v. 52, p. 659-672.

OWENS, L., AND C. KERANS, 2010, Revisiting the Cow Creek Limestone: facies architecture and depositional history of a greenhouse strandplain: Gulf Coast Association of Geological Societies Transactions, v. 60, p. 907-915.

SCOTT, R. W., 1993, Cretaceous carbonate platform, U.S. Gulf Coast, *in* Simo, J.A.T., Scott, R.W., and Masse, J.P., eds., Cretaceous carbonate platforms: American Association of Petroleum Geologists Memoir, v. 56, p. 97-109.

VERMEER, J., 2010, Mauritania, *in* Bird, E.C.F., ed., Encyclopedia of the World's Coastal Landforms, Springer Dordrecht, v. 1, p. 917-921.